# Design and Development of $Fe_3O_4/ZnTiO_3$/MWCNT/Epoxy Nanocomposite: An Integrated Experimental and Numerical Investigation of Microwave Impedance Matching and Scattering Parameters

**Mohammad Khakbaz[1]. Reza Sarkhosh[2*]. Masoud Javadi [3]**

*r.sarkhosh@modares.ac.ir

[1] Ph.D. Candidate, Department of Aerospace Engineering, Faculty of Graduate Studies, Shahid Sattari University of Aeronautical Sciences and Technology, Tehran, Iran

[2,3] Assistant Professor, Department of Aerospace Engineering, Shahid Sattari University of Aeronautical Sciences and Technology, Tehran, Iran

***Abstract:*** *Today, the application of high-performance thin-film nanocomposites as impedance-matching layers in telecommunication and military technologies has gained substantial importance. In this study, a multiphase nanocomposite comprising $Fe_3O_4$, $ZnTiO_3$, and multi-walled carbon nanotubes (MWCNT) embedded within an epoxy resin matrix was designed and synthesized under carefully controlled laboratory conditions. Experimental data were analyzed using multiple regression analysis alongside error variance reduction techniques to identify the optimal composition among the four finalized sample variants. During the fabrication process, the samples underwent sequential mixing, heating, and sonication steps to ensure proper dispersion of the fillers, followed by casting into molds with dimensions corresponding to the rectangular waveguide test section used for the electromagnetic measurements.Topological and morphological characterizations of the fabricated composites were performed by Scanning Electron Microscopy (SEM), while crystal structure assessments employed X-ray Diffraction (XRD) analysis. Furthermore, electromagnetic characterization was conducted using WR-90 waveguide measurements over the frequency range of 8.2–12.4 GHz. Among the samples examined, specimen C4, containing an increased $ZnTiO_3$ content, demonstrated superior particle dispersion and consequently improved electromagnetic impedance-matching performance. Numerical simulations carried out with the Frequency Domain Solver of CST Microwave Studio corroborated the experimental findings with considerable agreement. The results identified $Fe_3O_4$ as the dominant contributor to magnetic loss mechanisms, whereas MWCNTs served as conductive constituents within the composite matrix. The inclusion of $ZnTiO_3$ markedly enhanced impedance matching characteristics, resulting in a significant reduction of wave reflection and thereby facilitating improved wave energy transmission control across a broad bandwidth. Specifically, for the 1 mm thick C4 sample, the reflection coefficient was reduced to $-17.85$ dB, while the transmission parameter $S_{21}$ remained below $-0.072$ dB at 8.2 GHz, indicating excellent impedance matching and minimal reflective loss. Frequency-dependent analysis further demonstrated a stable balance between dielectric and magnetic contributions, manifesting in consistent electromagnetic performance without substantial deviation across the measured spectrum. Accordingly, the investigated nanocomposite emerges as a promising candidate for lightweight, high-performance absorber layers, impedance-matching layers, and electromagnetic coatings in advanced telecommunication and defense applications.*

***Keywords:*** *MWCNT/$Fe_3O_4$/$ZnTio_3$/Epoxy nanocomposite, Microwave Impedance Matching, S-Parameters, CST simulation, Waveguide measurements*

## 1. INTRODUCTION

In recent years, the development of new materials for electromagnetic (EM) wave absorption with reduced thickness, higher absorption efficiency, and wider operating bandwidths has been increasingly important. Thin absorbers play an important role in effectively mitigating both emitted and reflected antenna signals in communication systems to increase communication efficiency [1]. Recently, there have been attempts to improve ZnO semiconductor nanocomposites to increase microwave attenuation and shielding effectiveness as functional materials against electromagnetic interference (EMI) in various applications [2]. Mechanisms based on permittivity variations, along with the development of new materials, have been utilized.In general, two types of materials are used as absorbers: magnetic materials, such as ferrites, $Fe_3O_4$, and Fe, while ZnO, $TiO_2$, and SiC act as dielectric materials. The second type also includes lightweight carbon-based materials, including graphene, CNTs, and porous carbons. These materials often operate synergistically. Therefore, a synergistic interaction between magnetic and dielectric components enhances the efficiency of microwave absorbers. It also enables improvement in impedance matching and enhances attenuation performance over various frequency bands. Recently, attention has also been focused on using two-dimensional MXenes due to their high electrical conductivity and layered structural characteristics [3]. Core–shell nanostructured composites [4], especially those incorporating porous structures, also provide promising strategies for developing thinner and lighter microwave absorbers. These material systems provide a robust platform for the fabrication of absorbers suitable for next-generation electronics, communication systems, and aerospace applications.Polymeric nanocomposites [5], which possess conductive fillers and low-density matrices, combined



[ DOI: 10.22068/ijmse.4568 ]

with strong interfacial polarization, provide promising applications in microwave attenuation and EMI shielding. Effective structural design and optimized interactions between active materials and filler components are key factors in improving electromagnetic attenuation performance. The following review highlights current trends and emerging developments in polymer materials aimed at producing efficient microwave absorbers capable of mitigating electromagnetic pollution. Among various methods to counteract the effects of electromagnetic (EM) waves in various applications, microwave absorbing materials (MAMs) exhibit superior performance due to their inherent property of converting EM wave energy into thermal dissipation. Conventional materials comprising ferrites and ferric-based compounds often suffer from high density and limited stability. Recently, new materials based on lightweight carbon nanostructures like CNTs, CNFs, and CNMs have attracted significant attention due to their strong interfacial polarization and tunable dielectric properties. The addition of magnetic nanoparticles ($Fe_3O_4$ and Ni), along with dielectric materials such as SiC and $Ti_3C_2$ MXene, to CNTs and CNFs significantly improves magnetic–dielectric synergy and impedance matching. Moreover, according to recent studies conducted on graphene aerogels and carbon microspheres, their three-dimensional (3D) architectures facilitate multiple scattering and internal reflections, thus further enhancing energy dissipation. Consequently, well-designed carbon-based MAMs represent promising candidates for lightweight and high-efficiency electromagnetic absorption applications [6]. As illustrated by the schematic representation in Fig. 1, conductive, magnetic, and dielectric nanomaterials constitute the major classes of functional materials employed in advanced coating systems for military, defense, and communication applications.

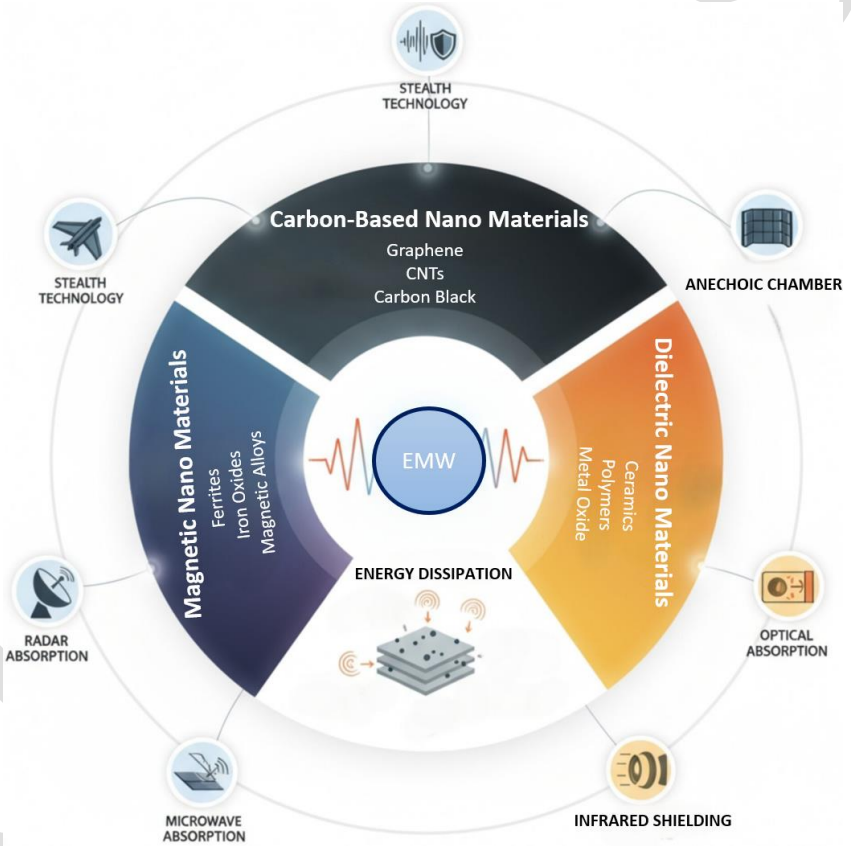


**Fig. 1.** Schematic illustration of the classification of commonly used nanomaterials applied in electromagnetic wave absorption and radar stealth coatings

Amongst the different metal oxides used to form the magnetic phase of nanocoatings, iron oxide nanoparticles such as magnetite ($Fe_3O_4$), maghemite ($\gamma$-$Fe_2O_3$), and hematite ($\alpha$-$Fe_2O_3$) are highly attractive due to their excellent magnetic properties, chemical durability, and ability to be manipulated with respect to particle size and crystal structures. Alternatively, when combined with carbon materials or dielectric materials, iron oxides show efficiency in microwave absorption and energy dissipation processes. In polymer-based nanocomposite structures such as $Fe_3O_4$@PPy, $Fe_3O_4$-$FeCO_3$/$FeCO_3$/MWCNTs/RGO, and $Fe_3O_4$@CuNW arrays, $Fe_3O_4$ is used as the magnetic core. The magnetic core generates interfacial polarization and magnetic-dielectric synergy, thus largely improving reflection loss and absorption bandwidths. The introduction of $Fe_3O_4$ nanoparticles simultaneously enhances



[ DOI: 10.22068/ijmse.4568 ]

impedance matching and magnetic resonance-based energy dissipation mechanisms. In particular, $Fe_3O_4$@PPy-A nanocomposites showed a −33.8 dB reflection loss at 11.5 GHz with 99.9% absorption efficiency, while their $Fe_3O_4$-C nanocomposite showed wide effective absorption bandwidths and lightweight properties. In another study, $Fe_3O_4$-MWCNT nanocomposites showed an impressive shielding efficiency value of about 60 dB at very thin thicknesses because of interfacial Fe-O-C bonds with enhanced electron transfer properties that increase interfacial dipole relaxation. In summary, magnetic $Fe_3O_4$-based nanomaterials are very important for the design of microwave absorption materials with high efficiency and low weight [7–10]. $Fe_3O_4$-based nanocomposites show highly efficient microwave absorption properties, especially in the Ku-band range, with well-matched impedance and iron oxide-based magnetic synergy, providing improved microwave absorption performance. In particular, the $Fe_3O_4$@$SiO_2$/MXene 3D superlattice structure enhances microwave propagation distances and interfacial polarization, with a reflection loss intensity of −60.9 dB at a thickness of 1.0 mm [11]. $Fe_3O_4$ nanofibers with electrospinning structures exhibit ferrimagnetic behavior with a high saturation magnetization of 58.4 emu/g and a coercivity of 186.7 Oe, with very high dielectric and magnetic losses from interfacial and exchange resonances, showing efficient microwave absorption in the 2–18 GHz frequency range, making them useful for lightweight microwave absorption materials [12]. As illustrated in Figure 2, electromagnetic signal attenuation occurs through $Fe_3O_4$-based nanofibers.

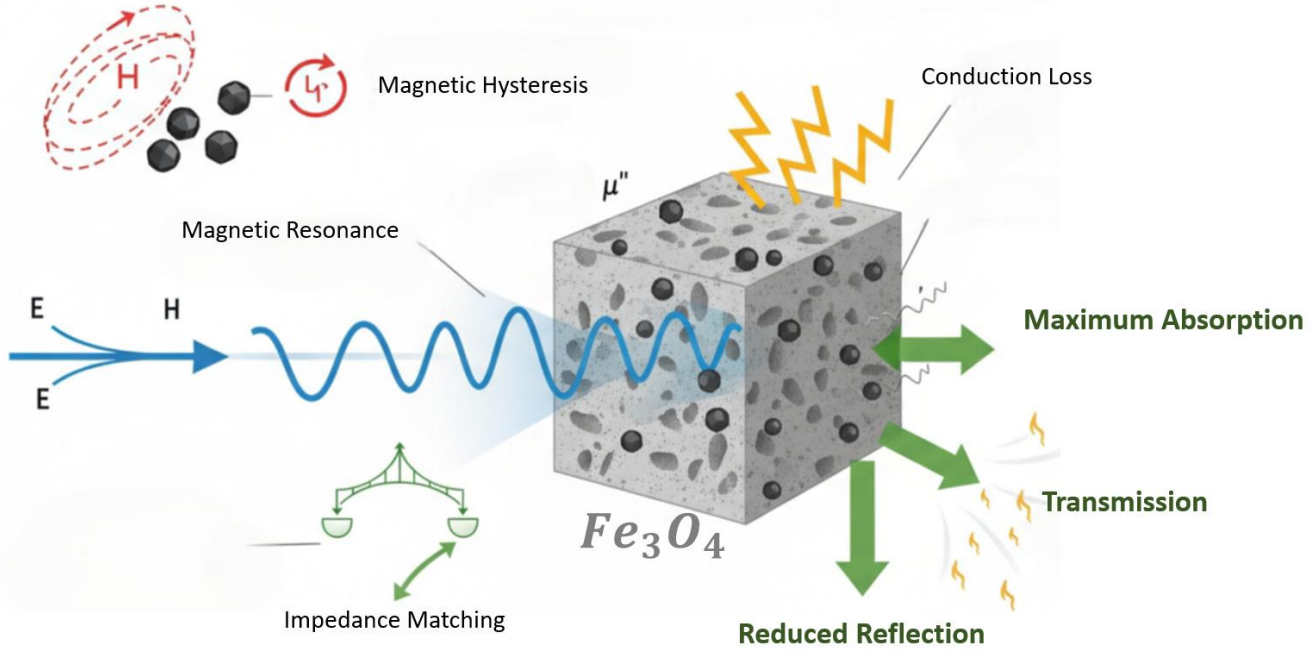


**Fig. 2.** Graphical schematic of the absorption and transmission effects of electromagnetic waves by $Fe_3O_4$ nanoparticles

The dielectric component plays a vital role in the absorption of electromagnetic waves. This is done by helping in the process of polarization relaxation and impedance optimization in nanocomposites. In the field of dielectric components, zinc titanate ($ZnTiO_3$) has a high dielectric constant, excellent thermal stability, and high dipole polarization. These properties make it a suitable material for absorption of electromagnetic waves and energy. Zinc titanate ($ZnTiO_3$) has excellent dielectric properties. The material has a high dielectric constant, low loss tangent ($<10^{-2}$), and excellent thermal stability. These properties make it suitable for the absorption of electromagnetic energy. The research study conducted on $ZnTiO_3$/epoxy nanocomposites has shown the presence of multiple polarization relaxation processes. The high interfacial and dipole polarizations make it superior to other polymers. Structural analysis revealed that the $ZnTiO_3$ compound, in the form of a combination of cubic and hexagonal structures, especially when calcined at 700 °C, shows the best results in terms of dielectric properties. Additionally, the modification of $ZnTiO_3$ by $Al_2O_3$ has the potential to control its dielectric properties by suppressing the loss tangent and improving the microstructures. A research study performed on $ZnTiO_3$ has shown its excellent potential for the successful fabrication of a microwave resonator. The replacement of $ZnTiO_3$ by up to 10 mol% of Ba, Ca, or Sr has shown excellent potential for the optimization of its dielectric properties. The partial substitution suppresses the formation of the rutile phase. The microwave property study has shown that the system has excellent microwave properties with a value of εr ranging between 25 and 32. The value of the quality factor, denoted by the symbol Q, varies between 2300 and 5400 at 10 GHz. The value of the tau-free layer, denoted by the symbol τf, varies between +56-22 ppm/°C. A research study conducted in 2021 stated that zinc titanate ($ZnTiO_3$) nanoparticles were synthesized



[ DOI: 10.22068/ijmse.4568 ]

by the microwave-assisted hydrothermal process to analyze their potential for solar cell technology. The findings of the research study concluded that $ZnTiO_3$ has the same starting point temperature at 500°C, and the dominant phase present at this temperature is the cubic form of $ZnTiO_3$ up to 800°C. The optical measurements conducted using the photoluminescence parameter have shown that the value of the photoluminescence intensity and the band gap energy increased. The phenomenon increased up to the maximum temperature of 700 °C, which has the highest proportion of cubic and rhombohedral phases of $ZnTiO_3$. The lowest value of synthesis energy expenditure is found at 500 °C. The study concluded that it has enormous potential for dye-sensitized solar cells. Zinc titanate ($ZnTiO_3$) nanomaterials have been synthesized by various traditional techniques, which include the sol-gel technique, the solid-state reaction technique, and the hydrothermal technique. Each process gives control over size, shape, and crystalline structure. Through sol-gel processing, precursors zinc acetate and tetrabutyl titanate have been mixed with chelating agents, namely benzene-1,3,5-tricarboxylic acid or stearic acid, to form well-defined $ZnTiO_3$ nanoparticles, which have a size of roughly 37-56 nm. This process enables a high degree of phase purity, where $ZnTiO_3$ is generated at a temperature of around 500°C, while a transformation from granular to fibrous morphology is observed from 800-1000°C. Characterization through XRD, FT-IR, and SEM analysis proves the formation of perovskite $ZnTiO_3$. $ZnTiO_3$ shows a high degree of photocatalytic performance, up to 70% degradation of methyl orange dye, when illuminated by UV light. This demonstrates its potential application in the realms of environmental and optoelectronic applications [18, 19].

MWCNTs represent one of the most efficient conductive fillers and the most effective methods for high electromagnetic wave-absorbing (EMA) performance because they possess high electrical conductivity, high aspect ratio, and good thermal stability. When introduced into the polymer matrix or nanocomposites, they form numerous conductive paths and interfaces, resulting in strong conductive losses and excellent microwave-absorbing capacity. According to previous studies, the introduction of multi-walled carbon nanotubes (MWCNTs) into the epoxy matrix can notably increase the electromagnetic wave-absorbing capacity in the composites due to their strong conductivity and aspect ratio, contributing to the efficient conductive network and leading to increased dielectric losses and, in some cases, simultaneous magnetic losses. Further advancements can be made through the control of morphology and interfaces, as shown in PPy/MWCNT composites through in-situ polymerization and subsequent doping treatment, where the three-dimensional conductive networks possess a rough morphology to form numerous interfaces and pore structures for extensive reflections and scattering of the electromagnetic waves, as well as enhanced interfaces for increased interfacial polarization and reinforced relaxation processes for increased polarization relaxation mechanisms, in combination with effective electron transport pathways for MWCNTs and PPy nanoparticles for increased conductivity losses and higher capacity for the dissipation of electromagnetic energy as heat. With the help of the dopant p-toluene sulfonic acid (TsOH), these PPy/MWCNT composites possess excellent EMA performance, demonstrating the strongest reflection loss value of –60.21dB at an operating frequency of 8.24GHz, together with an effective bandwidth for the entire thickness of up to 14.08GHz. Aside from the above nanosurface engineering, there is considerable proof for the critical effect contributed by microscale structure designs in the substantial enhancement in the capacity for electromagnetic wave-absorbing performance, as illustrated by the incorporation of the unique bowl-shaped polystyrene (PS) microspheres and the selective combination using the strong π-π interaction with the MWCNTs, in which the distinctive cavity structure can notably improve the impedance matching and extend the path lengths for the transiting electromagnetic wave and result in increased multiple internal reflections. Based on PS@MWCNT hybrids, the unique bowl-shaped PS@MWCNT nanocomposites possess strong electromagnetic wave-absorbing capacity, simplifying the reflection loss value to -34.92dB at an operating frequency of 13.01GHz for a thickness of 2.0mm and further reducing the entire thickness value to -38.57dB at an operating frequency of 14.04GHz for a thickness of 2.8mm, together with the effective bandwidth measuring up to 4.81GHz (amplitude: 6.45-11.26GHz). Furthermore, the research work conducted on epoxy resin/MWCNTs nanocomposites processed using an ultrasonic bath and milling process identifies that the optimum loading content of MWCNTs in both cases is 5 wt% and 15 wt%, respectively. Also, the values of reflection loss as low as −25 dB have been achieved for the ultrasonic-dispersed sample within the range 9-11 GHz due to their efficient dispersion and interfacial polarization. These results establish that MWCNTs act as conducting paths as well as polarization sites, which play a major role in ensuring impedance matching, energy loss, and efficient microwave absorption for nanocomposites. [20-23].

Although conductive and magnetic fillers such as MWCNTs and $Fe_3O_4$ have been extensively explored, achieving simultaneous impedance matching and broadband absorption remains challenging. Previous studies predominantly enhanced conductive or magnetic loss pathways individually, with limited attention to the dielectric regulation necessary to balance these mechanisms. In this context, $ZnTiO_3$ a perovskite oxide with high permittivity and strong dipolar polarization has rarely been employed in hybrid absorbers despite its significant potential as a dielectric-tuning phase. The present work addresses this gap by developing a $Fe_3O_4$/$ZnTiO_3$/MWCNT/epoxy multiphase nanocomposite and evaluating how precisely controlled $ZnTiO_3$ loading modulates dielectric behavior



[ DOI: 10.22068/ijmse.4568 ]

and overall microwave absorption. Through a comprehensive workflow involving material design, fabrication, morphological analysis, optimization, and numerical simulation, the presence and functional contribution of $ZnTiO_3$ are clearly demonstrated.

## 2. GOVERNING EQUATIONS

The process of characterizing the electromagnetic properties of nanocomposite materials for microwave absorption applications begins by measuring scattering parameters (S-parameters) with a vector network analyzer. From these measurements, complex permittivity and permeability are obtained using the Nicholson-Ross-Weir (NRW) method [24-27], which ultimately allows for the calculation of reflection loss performance for both single-layer and multi-layer absorber configurations. The scattering matrix is defined by Equation (1):

$$S = \begin{bmatrix} S_{11} & S_{12} \\ S_{21} & S_{22} \end{bmatrix} \tag{1}$$

where $S_{11}$ and $S_{22}$ represent the reflection coefficients for ports 1 and 2, respectively, while $S_{12}$ and $S_{21}$ indicate the transmission coefficients between the two ports. When a nanocomposite sample of a certain thickness is placed in a coaxial transmission line [28], the measured reflection coefficient and transmission coefficient contain complete information about the material's electromagnetic response. The NRW algorithm begins by calculating the interface reflection coefficient using an intermediate parameter constructed from the S-parameters:

$$K = \frac{S_{11}^2 - S_{21}^2 + 1}{2S_{11}} \tag{2}$$

$$\Gamma = K \pm \sqrt{K^2 - 1} \tag{3}$$

where $K$ serves as a dimensionless variable that facilitates the mathematical extraction process, represents the complex reflection coefficient at the interface between air and the material (with a magnitude for passive materials as a result of energy conservation), and the sign in equation (3) is selected to comply with the passivity constraint. The transmission coefficient across the sample, which considers multiple internal reflections, is then derived as:

$$T = \frac{S_{11} + S_{21} - \Gamma}{1 - (S_{11} + S_{21})\Gamma} \tag{4}$$

where $T$ represents the complex transmission coefficient incorporating both phase delay and attenuation through the material thickness. From the transmission coefficient, the complex propagation constant $\gamma = \alpha + j\beta$ is extracted, where $\alpha$ is the attenuation constant in Np/m representing exponential amplitude decay, and $\beta$ is the phase constant in rad/m:

$$\gamma = \frac{1}{d}\ln\left(\frac{1}{T}\right) \tag{5}$$

The characteristic impedance of the nanocomposite material is calculated from:

$$Z = Z_0\sqrt{\frac{(1+\Gamma)^2 - T^2}{(1-\Gamma)^2 - T^2}} \tag{6}$$

Where Z represents the complex characteristic impedance measured in ohms, and $Z_0 = 377\ \Omega$ refers to the impedance of free space. This value signifies the relationship between the transverse electric field and the magnetic field components in the wave that is propagating. After obtaining the complex relative permittivity $\mu_r = \mu'_r - j\mu''_r$ and permeability $\varepsilon_r = \varepsilon'_r - j\varepsilon''_r$, they are extracted using basic electromagnetic relations.

$$\varepsilon_r = \varepsilon'_r - j\varepsilon''_r = \frac{\gamma c_0}{j\omega Z_0 Z} \tag{7}$$

$$\mu_r = \mu'_r - j\mu''_r = \frac{\gamma Z c_0}{j\omega Z_0} \tag{8}$$

where $\varepsilon'_r$ is the real permittivity (dielectric constant) representing electric energy storage through polarization mechanisms (electronic, ionic, dipolar, interfacial), $\varepsilon''_r$ is the imaginary permittivity representing dielectric losses from conduction and relaxation, $\mu'_r$ is the real permeability representing magnetic energy storage through magnetization (domain wall motion, domain rotation, spin rotation in magnetic nanoparticles), $\mu''_r$ is the imaginary





[ DOI: 10.22068/ijmse.4568 ]

permeability representing magnetic losses from hysteresis, eddy currents, and ferromagnetic resonance, $\omega = 2\pi f$ is the angular frequency in rad/s, and $c_0 = 10^8 m/s$ is the speed of light.
The reflection loss, which is the primary performance metric for microwave absorbers expressed in decibels, is calculated from the input impedance [30]:

$$RL_{dB} = 20\ log_{10} \left| \frac{Z_{in} - Z_0}{Z_{in} + Z_0} \right| \tag{9}$$

where the value of RL is consistently negative for passive materials, with increasingly negative values indicating improved microwave attenuation, absorption and effective impedance matching performance.

## 3. EXPERIMENTAL METHOD

### 3.1. Design of Experiment

To investigate the influence of dielectric content on the electromagnetic behavior of the nanocomposite, four formulations (C1–C4) were prepared with controlled variations in the weight fractions of epoxy resin, $ZnTiO_3$, MWCNTs, and $Fe_3O_4$ nanoparticles. The experimental design was guided by Response Surface Methodology (RSM), which incorporates regression modeling, variance analysis, and statistical error evaluation to assess the contribution of individual components and improve parameter selection. In this design, $ZnTiO_3$ was selected as the primary variable because of its role as a dielectric tuning phase that influences polarization mechanisms and impedance matching within the composite. Accordingly, the $ZnTiO_3$ content was varied from 10.28 to 19.67 wt%. To maintain the total composition at 100 wt%, the epoxy resin content was adjusted correspondingly from 55.42 to 45.18 wt%. In contrast, the contents of MWCNTs and $Fe_3O_4$ were maintained within relatively narrow ranges of 9.71–10.22 wt% and 24.49–25.55 wt%, respectively. This constrained variation was intentionally adopted to preserve stable conductive and magnetic loss mechanisms while preventing excessive conductive percolation or dominant magnetic attenuation that could mask the dielectric tuning effect of $ZnTiO_3$. Additionally, microwave electromagnetic properties of multiphase nanocomposites are known to be highly sensitive to small compositional variations; therefore, even minor adjustments within this range can produce measurable changes in the effective electromagnetic response. The final compositions of all samples are summarized in Table 1. Statistical descriptors including mean, median, variance, standard deviation, and covariance were calculated for each component, and the results are presented in Table 2. Among the investigated constituents, $ZnTiO_3$ exhibited the highest variance (14.58) and a standard deviation of 3.82, confirming that it represents the primary variable in the experimental design. Conversely, epoxy resin showed a strong negative covariance (−16.93) with $ZnTiO_3$, reflecting the compensatory adjustment required to maintain the overall composition balance. The statistical characteristics of the dataset are further illustrated in Fig. 3 through histogram distributions, box plots, and correlation analysis. The histogram plots indicate approximately normal distributions for $ZnTiO_3$ and epoxy contents, while the MWCNT and $Fe_3O_4$ values remain tightly clustered, consistent with the controlled design constraints. The box plots demonstrate that the spread of $ZnTiO_3$ content is approximately 9 wt%, highlighting its role as the principal tuning parameter in the composite formulation. Correlation analysis further reveals a strong inverse relationship between $ZnTiO_3$ and epoxy contents ($r \approx -0.97$), whereas the correlations among the remaining components remain weak ($r < 0.2$), indicating that they were varied independently within the design limits. Overall, this experimental framework enables a statistically controlled evaluation of how dielectric tuning through $ZnTiO_3$ influences the electromagnetic response of the $Fe_3O_4$/$ZnTiO_3$/MWCNT/epoxy nanocomposite system while maintaining stable conductive and magnetic loss contributions.

**Table 1.** Suggested mass percentage values for each material

| Sample | Resin Epoxy (wt%) | $ZnTio_3$ (wt%) | MWCNT (wt%) | $Fe_3O_4$ (wt%) |
|---|---|---|---|---|
| C1 | 55.42 | 10.28 | 9.71 | 24.49 |
| C2 | 51.36 | 13.85 | 9.24 | 25.55 |
| C3 | 48.72 | 16.42 | 10.13 | 24.73 |
| C4 | 45.18 | 19.67 | 10.22 | 24.93 |



[ DOI: 10.22068/ijmse.4568 ]

**Table 2.** Statistical indicators (based on mass percentage of each component)

| Component | Mean | Median | Variance | .Std. Dev | Covariance (w/$ZnTio_3$) |
|---|---|---|---|---|---|
| Resin | 50.17 | 50.04 | 17.07 | 4.13 | -16.93 |
| $ZnTio_3$ | 15.56 | 15.13 | 14.58 | 3.82 | +14.58 |
| MWCNT | 9.83 | 9.97 | 0.19 | 0.44 | +0.13 |
| $Fe_3O_4$ | 24.95 | 24.83 | 0.23 | 0.48 | -0.17 |

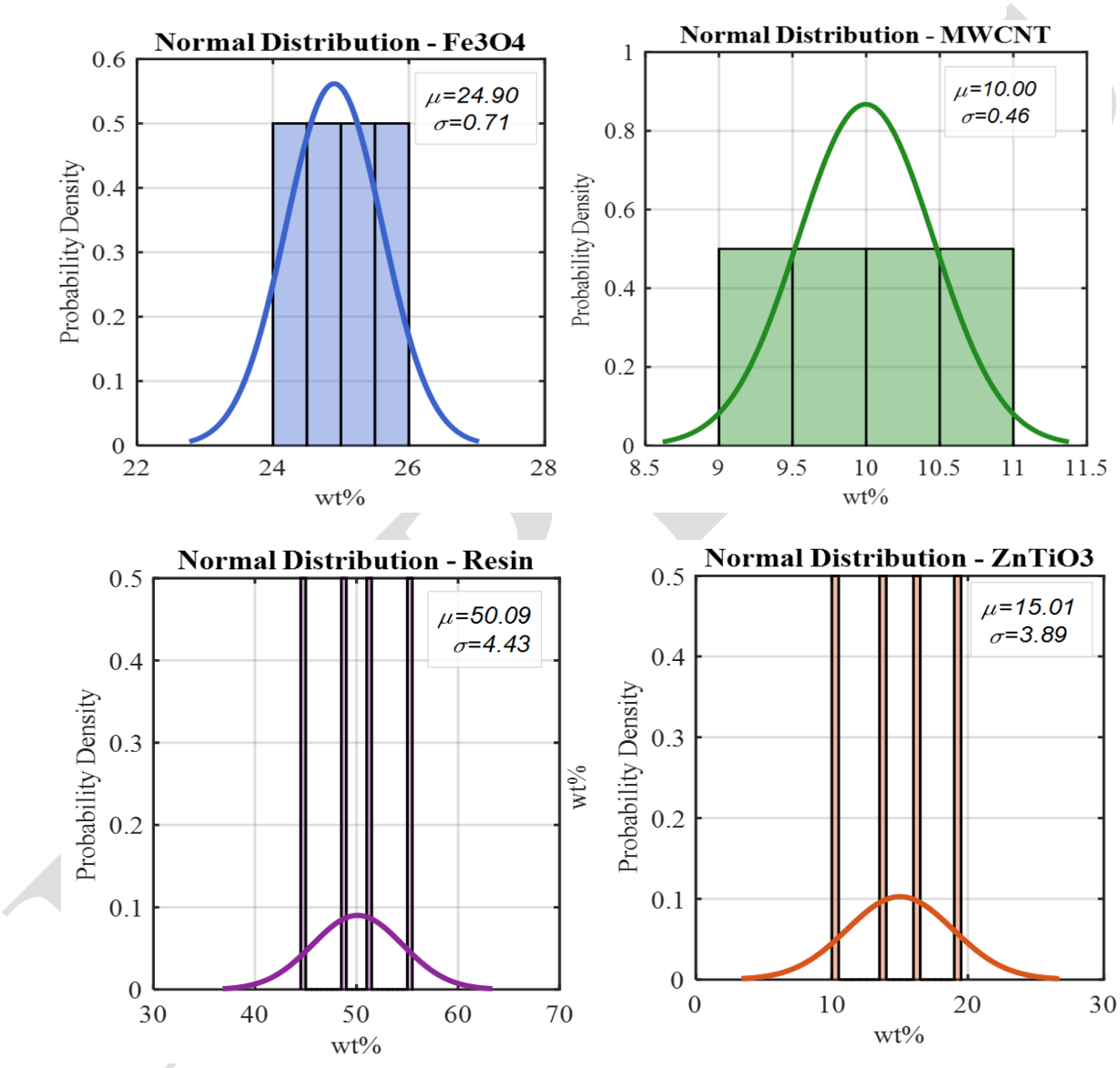


**Fig. 3.** Statistical Visualization of $Fe_3O_4$/$ZnTiO_3$/MWCNT/Epoxy System

### 3.2. Fabrication Process of $Fe_3O_4$ /$ZnTiO_3$/MWCNT/ Nanocomposite

As per the experimental design discussed in Section 3.1, the nanopowder mixture of $Fe_3O_4$, $ZnTiO_3$, and MWCNT in the nanocomposite $Fe_3O_4$/$ZnTiO_3$/MWCNT/epoxy was appropriately mixed in the lab under controlled conditions. The high-purity nanopowders of $Fe_3O_4$, $ZnTiO_3$, and MWCNTs were commercially acquired in laboratory-grade form. According to the manufacturer's specifications, the $Fe_3O_4$ and MWCNTs were produced via the chemical vapor deposition (CVD) method, while the $ZnTiO_3$ was synthesized using the sol-gel process. Following the experimental



[ DOI: 10.22068/ijmse.4568 ]

design discussed in Section 3.1, these nanopowders were then precisely blended into the epoxy resin matrix in our laboratory under controlled conditions to ensure a homogeneous distribution."To start the process, the measured amount of $ZnTiO_3$, $Fe_3O_4$, and MWCNTs, according to the experimental design matrix, was mixed in ethanol. This mixture was heated at 100 °C and stirred at a rate of 100 rpm using a magnetic stirrer to ensure uniform distribution of the nanoparticles in the solvent. To ensure good distribution of the nanoparticles and avoid aggregation, the mixture was treated with ultrasonication for a period of 25 minutes, with ice pieces in the ultrasonic chamber to prevent overheating of the mixture and ensure that the nanoscale properties are maintained and preserved. After ultrasonication, the mixture was carefully stirred at a moderate rate at high temperature and allowed some solvent to evaporate. As a result, the mixture viscosity increased in preparation for mixing with epoxy resin. At the same time, a bisphenol-A-type epoxy resin (Epon 828) was preheated at a lower temperature in readiness for easier mixing with nanopowders. A mixture of the nanopowder suspension and the preheated epoxy resin was prepared while stirring the mixture. As a result, a uniform mixture was created. After that, the mixture was maintained at a temperature of 100 °C until all the ethanol had evaporated. After that, the mixture showed viscosity and uniformity in readiness for further processing. After slight cooling, the hardener, triethylenetetramine (TETA), was mixed in a ratio of 2:1 (resin-hardener ratio). At that point, the mixture was ready for further processing. It was poured into molds and allowed to solidify at room temperature. After that, the mixture was fully solidified, and there was no need for further heating for hardening, as at that point, the ambient temperature was sufficient for the completion of hardening of the epoxy matrix. Figure 4 shows the lab-scale fabrication process in detail. The key processes involved in this step range from nanoparticle dispersion and ultrasonication to the mixing of the dispersion with the epoxy matrix and molding. The entire process requires specific control over temperatures and sonication for an effective nanocomposite formation.


**Fig. 4.** Experimental procedure for laboratory-scale nanocomposite fabrication



[ DOI: 10.22068/ijmse.4568 ]

## 4. CHARACTERIZATION

With respect to the analysis of the prepared nanocomposite, scanning electron microscopy (SEM) analysis was c onducted on the surface morphology of the $ZnTiO_3/Fe_3O_4$/MWCNT/epoxy nanocomposite. This was in relation to t he observation of the dispersed morphology of the $ZnTiO_3/Fe_3O_4$/MWCNTs in the epoxy matrix of the prepared co mposite material. Additionally, the crystalline structure of the hybrid composite was analyzed through the use of X-ray diffraction (XRD) analysis. With a magnification range of 500nm, the SEM micrographs offer in-depth informa tion about the microstructure characteristics of the nanocomposite material. The micrographs indicate the existence of neatly distributed granular and plate-like regions that can be identified as $ZnTiO_3$ and $Fe_3O_4$ nanoparticles dispers ed in the epoxy matrix. The nanoparticles display an average homogeneous distribution with minimal agglomeratio n, signifying optimized processing and high compatibility between the inorganic nanoparticles and the epoxy matrix . In addition, the distinct boundaries between the nanoparticles and the epoxy region provide an indication of high i nterfacial adhesion and mechanical locking, which can be attributed to efficient stress transfer. The display of fractu red boundaries and rugged surfaces further confirms the development of an integrated structure. However, the few microvoids detectable in the structure would most probably be attributable to the shrinkage that takes place during t he curing process. A higher magnification at a scale of 200 nm, as seen from the SEM micrographs, displays more r efined structural features, such as a uniform dispersion of nanoparticles, which have an average size ranging from 3 0-40 nm. It is noteworthy that both $Fe_3O_4$ and $ZnTiO_3$ nanoparticles are seen to be attached to the surfaces of MWC NTs, giving rise to a hybrid network. The above-mentioned micrograph reveals an effective interaction at the surfac es of MWCNTs and attached nanoparticles, which leads to successful load transfer and brings about conductivity an d magnetization pathways across the surfaces of the neat epoxy. A similar synergistic effect would be responsible fo r contributing towards an improvement in the mechanical, electromagnetic, and multifunctional properties of the na nocomposite material. In conclusion, based on the SEM results at the 500 nm and 200 nm scales, the uniform disper sion, strong interfacial affinity, and tightly integrated hybrid structure of $ZnTiO_3$, $Fe_3O_4$, and MWCNT nanofillers i n the epoxy resin not only effectively enhance the dispersed phase but also significantly impact the resultant propert ies of the synthesized nanocomposite. The images presented in Fig. 5 show SEM images of how nanocomposite par ticles are dispersed at different magnifications.

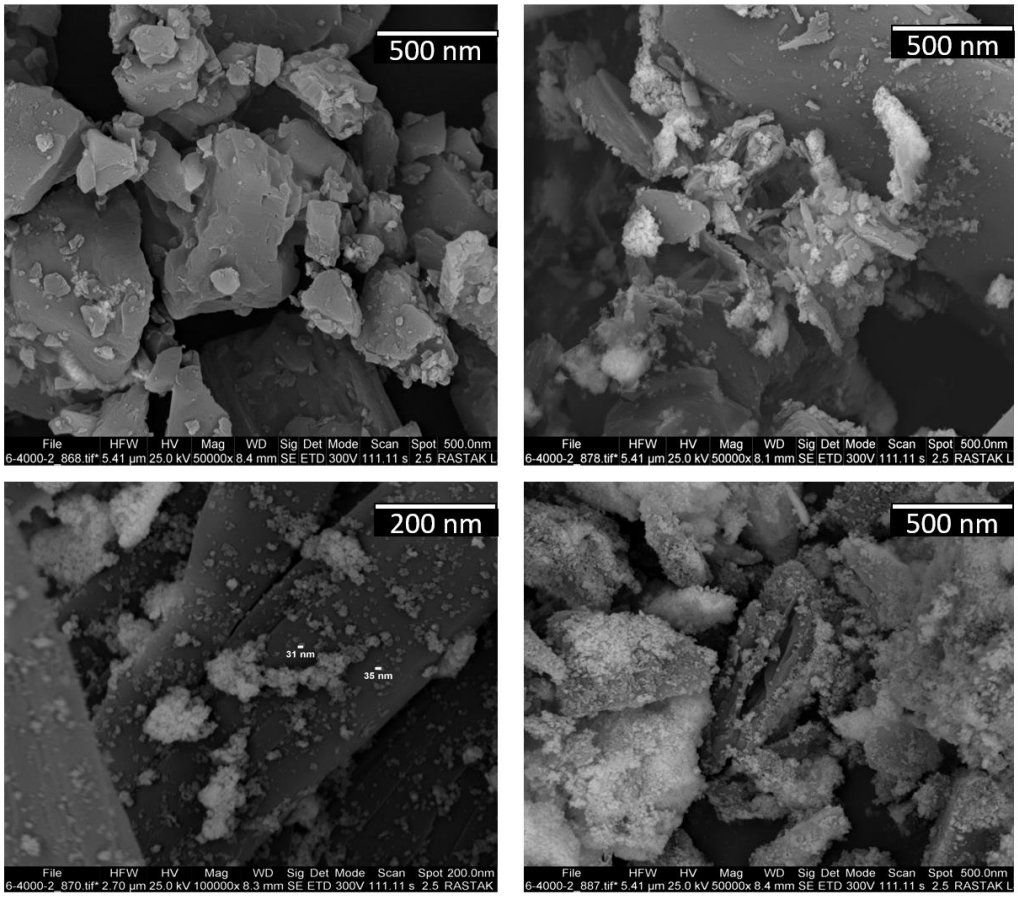




[ DOI: 10.22068/ijmse.4568 ]

**Fig. 5.** SEM images at different sizes to show the dispersion of nanoparticles in the matrix

As illustrated in Fig. 6, the X-ray diffraction (XRD) pattern of the $Fe_3O_4/ZnTiO_3$/MWCNT/epoxy nanocomposite shows that the $Fe_3O_4$ peaks with $2\theta \approx 30.1°$, 35.5°, and 43.2° have less intense peak values and are broader compared to the pure material. This phenomenon can render the size of the crystallite smaller by about 10nm, with increased interphase strain. The diffraction peaks for the $ZnTiO_3$ phases with $2\theta \approx 31.8°$, 34.4°, and 36.2° are also manifested, but with increased broadness and less intensity, estimating the crystallite size to be around 8-9nm. The (002) plane diffraction peak for the MWCNT with $2\theta \approx 26°$ is broad, moderately intense, and points to the possibility of the layering height being about 2nm with the presence of some level of turbostratic disorder. The broad diffraction peak for the epoxy with $2\theta \approx 18°$ confirms the material to have an amorphous structure. The broadening of the diffraction peak for the nanocomposites compared to the individual phases points to physical blending, increased interphase straining, and lower crystallinity. The size of the crystallites, using the Scherrer formula, revealed $Fe_3O_4$ to have the highest crystallinity, while $ZnTiO_3$ is second, with MWCNT having the least crystallinity. The differences in the FWHM values, with the reduction in intensities, reflect the trend of the crystallite size tending to vary more with increased particle distribution. Thus, the nanocomposites have reduced crystallinity with unique peak width and size changes.

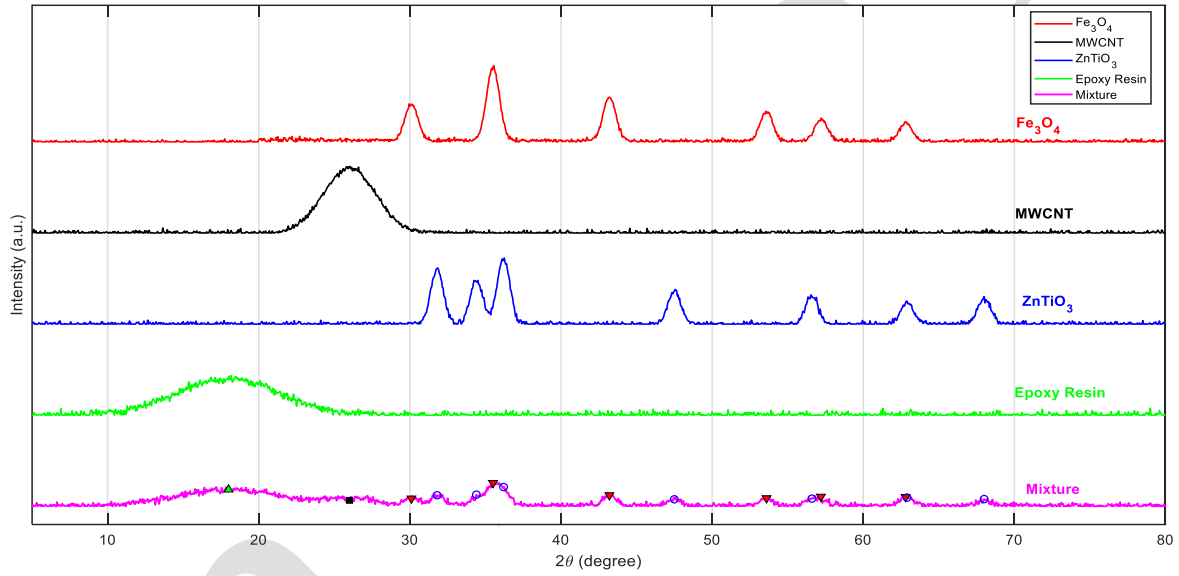


**Fig. 6.** X-ray diffraction patterns of individual components and the resulting nanocomposite mixture

The VSM hysteresis diagram illustrated in Fig. 7 depicts a magnetic nanocomposite made up of a multiphase comp osition that includes magnetic ferrite particles ($Fe_3O_4$), semi-magnetic or weakly magnetic materials such as $ZnTiO_3$, carbon nanotubes (MWCNTs), and a non-magnetic matrix. The hysteresis diagram indicates that $Fe_3O_4$ particles significantly contribute to achieving a high magnetic moment and rapid saturation characteristics, while $ZnTiO_3$, du e to its weaker magnetic traits, results in gradual variations in the hysteresis curve, resulting in a smoother overall magnetic response. The inclusion of MWCNTs introduces diamagnetic effects and slightly reduces the overall mag netic moment, but they also enhance heat transfer and the mechanical stability of the composite, whereas the non-m agnetic matrix preserves the physical structure and governs the particle dispersion.The interplay of these different p hases leads to a nonlinear, multi-stage magnetic behavior that approaches relative saturation as the external magneti c field increases.



[ DOI: 10.22068/ijmse.4568 ]

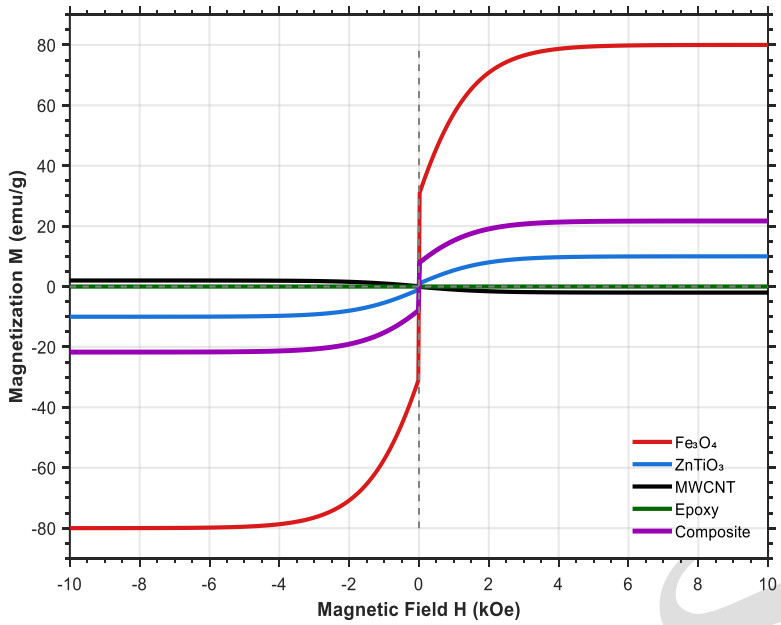


**Fig. 7.** Hysteresis loop of multiphase magnetic nanocomposite: Role of $Fe_3O_4$, $ZnTiO_3$, and MWCNT in the composite magnetic behavior

## 5. VNA SETUP

The experimental setup for evaluating the electromagnetic characteristics of the nanocomposites within the X-band frequency range (8.2–12.4 GHz) consisted of a microwave source providing a controlled input power of +20 dBm. The generated signal was fed into a standard WR-90 rectangular waveguide with internal cross-sectional dimensions of 22.86 × 10.16 mm². The waveguide length was designed to accommodate the samples while minimizing reflections from the terminations.

The incident microwave signal first passed through a two-port directional coupler, enabling independent and simultaneous monitoring of the forward and reflected powers. Subsequently, the wave was directed into a customized sample holder containing four nanocomposite specimens. These specimens were machined to precisely match the waveguide cross-section and limited in thickness along the dominant $TE_{10}$ propagation mode. The samples were firmly attached to the waveguide walls without air gaps to minimize scattering and ensure uniform field distribution.

The transmitted signal was connected to port 2 of a Vector Network Analyzer (VNA), while the reflected signal was linked to port 1, allowing accurate measurement of the $S_{11}$ and $S_{21}$ parameters corresponding to the reflection and transmission responses, respectively. Each sample was measured three times, and the averaged S-parameter data were employed for further analysis.

The entire measurement system was calibrated using the SOLT (Short–Open–Load–Through) method. The sample holders were fabricated from non-magnetic, low-loss dielectric materials to minimize undesired reflections and insertion losses. This configuration ensured accurate and repeatable measurements for evaluating the scattering, reflection, and transmission characteristics of the prepared nanocomposites. Figure 8 schematically illustrates the waveguide experimental setup used for the four fabricated samples (C1–C4).



[ DOI: 10.22068/ijmse.4568 ]

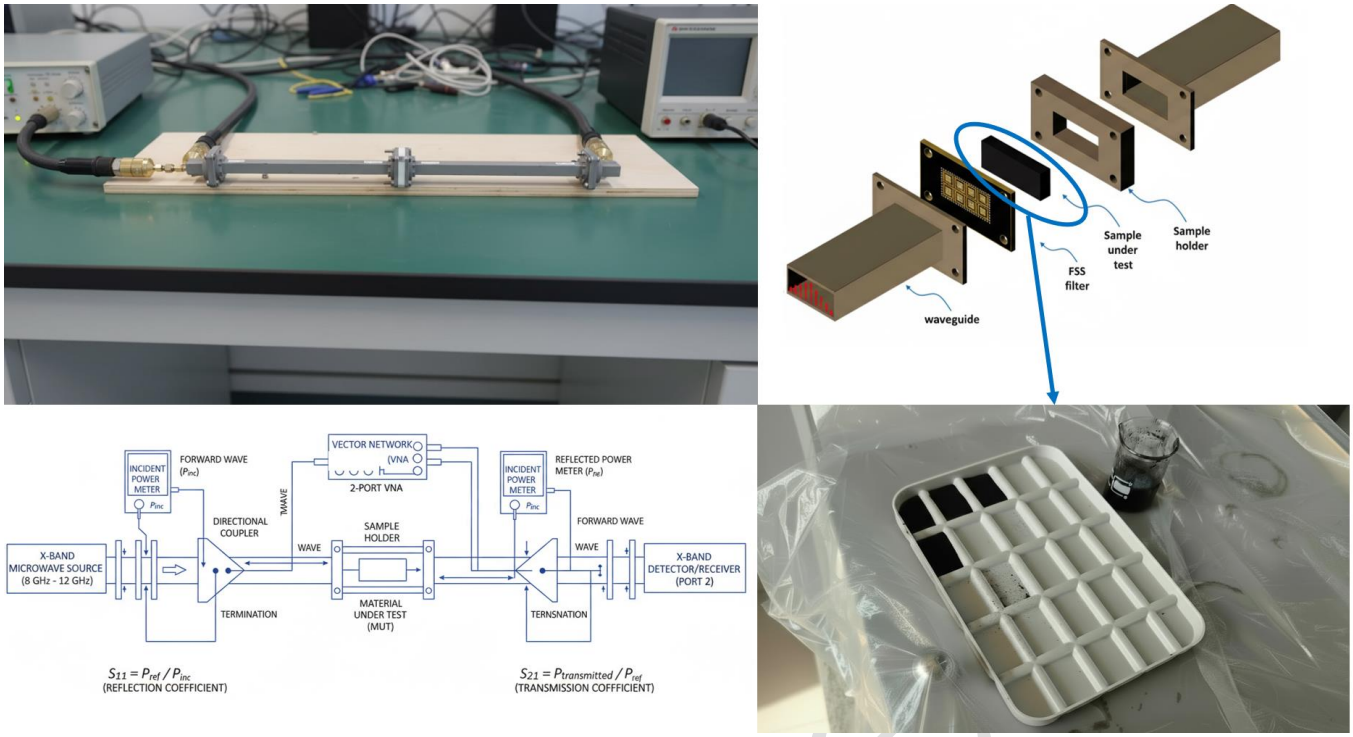


**Fig. 8.** Waveguide experimental setup for measuring the electromagnetic properties of the four nanocomposite samples (C1–C4)

## 6. NUMERICAL SIMULATION

To perform the numerical simulation of the waveguide configuration incorporating the nanocomposite material, CST Studio Suite 2021 was employed within the Microwave Studio environment using the Frequency Domain Solver. This approach enabled an accurate evaluation of the electromagnetic response and reflection coefficient of the sample over the X-band frequency range (8.2–12.4 GHz). A standard WR-90 waveguide, with internal cross-sectional dimensions of 22.86 × 10.16 mm², was modeled to represent the measurement configuration.
The nanocomposite, consisting of MWCNTs, $Fe_3O_4$, $ZnTiO_3$, and an epoxy matrix, was introduced into the waveguide as a homogeneous layer with a thickness of 1 mm, positioned at the center of the structure along the propagation direction (z-axis). This configuration was selected to realistically simulate the interaction between the incident microwave fields and the composite material.To ensure numerical accuracy and solution stability, an adaptive hexahedral meshing scheme was applied. This method allowed for refined mesh control in regions exhibiting strong electromagnetic field gradients. Within the nanocomposite domain, a minimum of twenty mesh cells per effective wavelength was enforced, while additional mesh refinement was automatically applied near the material–waveguide interfaces to accurately capture rapid spatial variations of the electric and magnetic fields. The boundary conditions in the transverse directions were defined according to the field distribution of the dominant $TE_{10}$ mode. Accordingly, $E_t = 0$ was imposed at the xmin and xmax boundaries, while $H_t = 0$ was applied at the ymin and ymax boundaries. Along the propagation direction, open boundary conditions were assigned to suppress spurious reflections from the waveguide terminations and to emulate realistic wave propagation. Two standard waveguide ports were defined at the input and output ends of the structure for field excitation and detection. The dominant $TE_{10}$ mode was excited at the input port with an input power of 1 W, providing proper energy normalization and enabling direct comparison of the simulated reflection ($S_{11}$) and transmission ($S_{21}$) parameters with the experimental VNA measurements. The output port was configured as a power monitor, and both field distributions and power flow data were collected at the two ports. The effective electromagnetic properties of the nanocomposite, including effective permittivity ($\varepsilon_{eff}$), permeability ($\mu_{eff}$), conductivity ($\sigma_{eff}$), and density ($\rho_{eff}$), were estimated using weighted averaging based on the mass fractions of the constituent phases. Effective medium theories, including the Maxwell–Garnett [31] and Halpin–Tsai [32] models, were employed to account for interfacial polarization effects, the percolation behavior of the MWCNT conductive network, and the magnetic contributions of $Fe_3O_4$ particles. The resulting parameters were implemented in the CST material library as a frequency-dispersive lossy material, allowing accurate reproduction of the composite's frequency-dependent dielectric and magnetic responses. Figure 9 illustrates the


[ DOI: 10.22068/ijmse.4568 ]

schematic of the waveguide simulation model with the nanocomposite layer inserted into the structure. The electromagnetic excitation and monitoring at the waveguide ports are defined to extract the scattering parameters and assess the overall electromagnetic performance of the nanocomposite within the numerical framework.

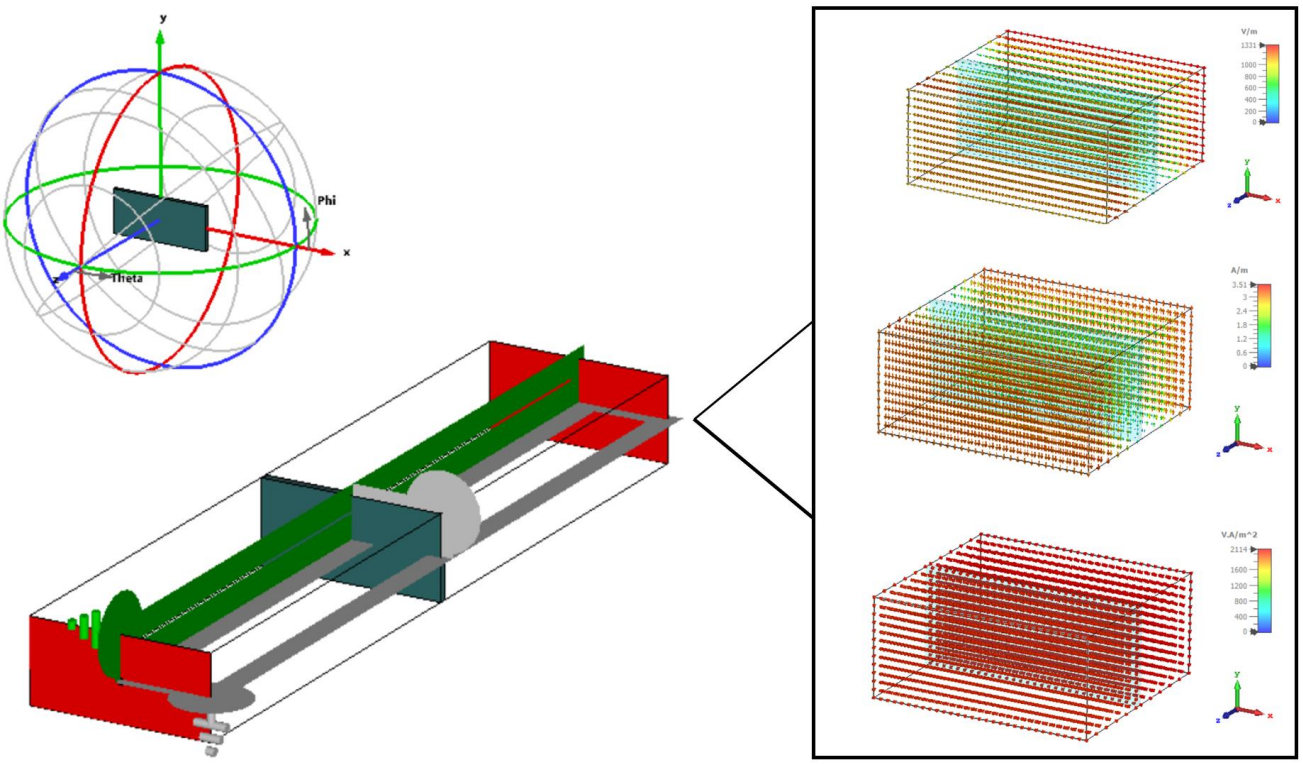


**Fig. 9.** Computational model illustrating the imposed boundary conditions, transmitting and receiving ports, and the spatial distributions of electric and magnetic fields for the nanocomposite structure within the full-wave electromagnetic simulation framework

During the post-processing phase, the S-parameters ($S_{11}$ and $S_{21}$) were analyzed within the Result Template Manager to derive the frequency-dependent reflection and transmission characteristics of the fabricated nanocomposite layer. Furthermore, far-field radiation patterns were extracted at regular frequency intervals throughout the X-band for each port, allowing a comprehensive evaluation of the angular distributions of the scattered and transmitted electromagnetic fields. This approach facilitated the investigation of field propagation, potential leakage, and modal behavior within the waveguide when interacting with the composite layer. The simulation framework, which combines accurate geometric modeling, effective multicomponent electromagnetic properties, adaptive hexahedral meshing, controlled excitation, and far-field analysis at selected frequencies, provides a robust numerical approach for predicting the attenuation and transmission behavior of nanocomposite materials. Figure 10 presents the far-field contour distributions for each port at representative frequencies of 8.2, 10, and 12.4 GHz, illustrating the frequency-dependent variation of the radiated field patterns within the X-band. The simulated results exhibit a strong correlation with the reflection reduction observed in the experimental waveguide measurements, confirming the reliability of the numerical model in reproducing the electromagnetic response of the fabricated sample.

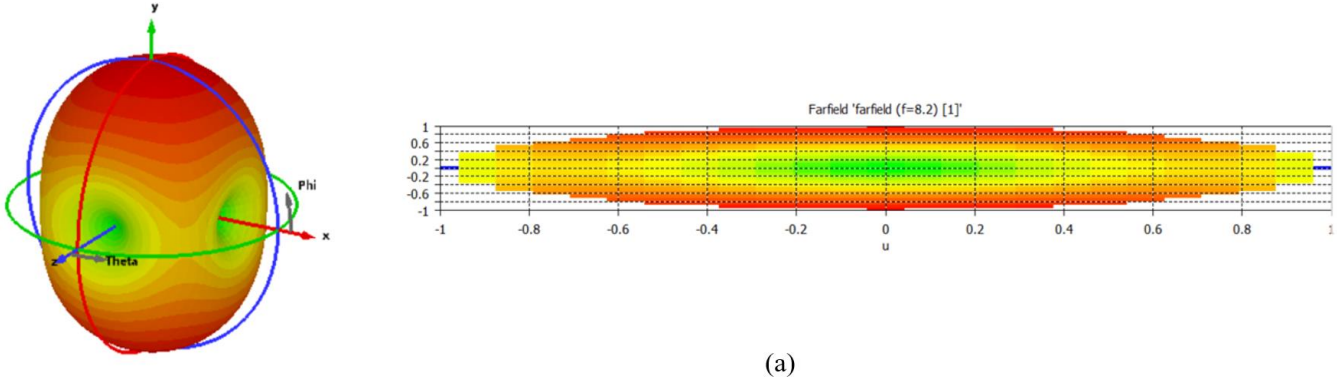


(a)



[ DOI: 10.22068/ijmse.4568 ]

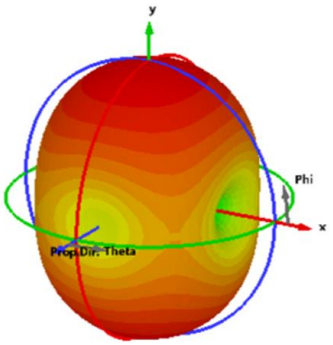


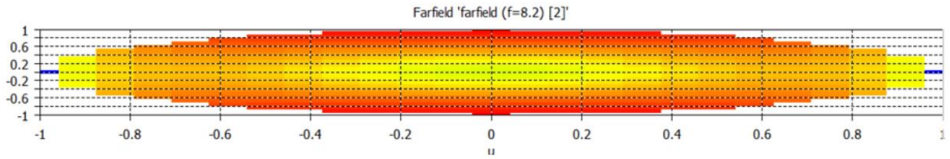


(b)

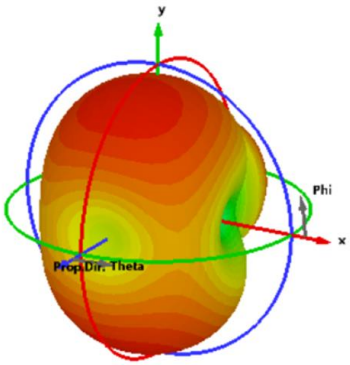


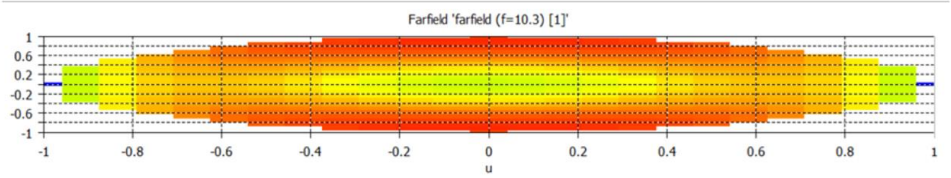


(c)

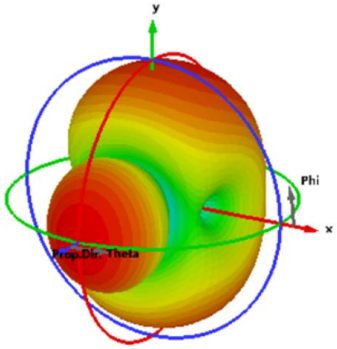


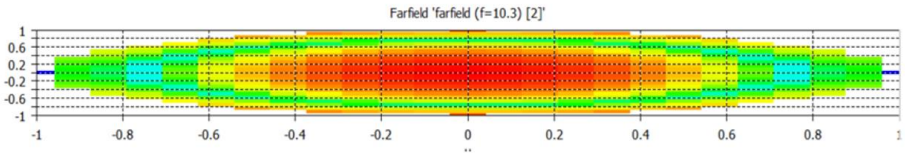


(d)

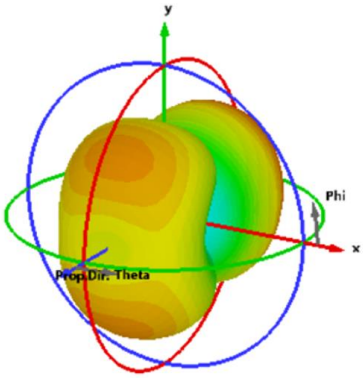


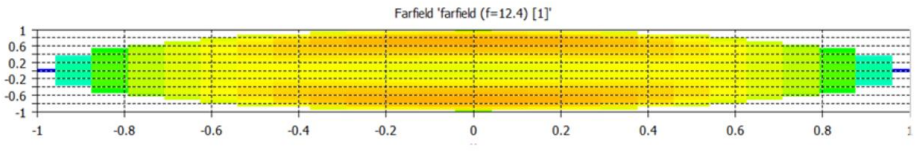


(e)

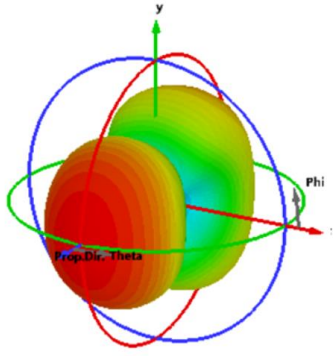


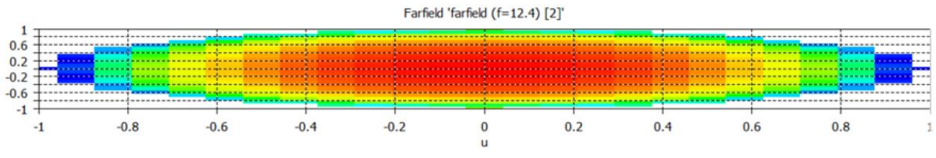


(f)



[ DOI: 10.22068/ijmse.4568 ]

**Fig. 10.** Figure X. Angular far-field 3D contour plots illustrating the radiation distribution for Port 1 and Port 2 at selected even frequencies: (a) Port 1 at 8.2 GHz, (b) Port 2 at 8.2 GHz, (c) Port 1 at 10 GHz, (d) Port 2 at 10 GHz, (e) Port 1 at 12.4 GHz, and (f) Port 2 at 12.2 GHz.

## 7. RESULTS AND DISCUSSION

### 7.1. Scattering Parameters of Numerical Solution

As depicted from the data presented in Table 3 and the corresponding graphical illustrations in Figures 11 through 1 4, the simulated nanocomposite based on the optimal composition derived from prior experiments demonstrates pre dictable, stable, and consistent performance across the entire frequency range from 8.2 GHz to 12.4 GHz. The frequ ency-dependent variation of the reflection coefficient $S_{11}$ of the proposed structure, obtained via a numerical solutio n using the CST software platform, is shown in Figure 11. Simulation results indicate that in the lower frequency ba nd between 8.2 GHz and 9.5 GHz, the magnitude of $S_{11}$ remains low, ranging from −16.17 dB at 8.2 GHz to −15.04 dB at 9.5 GHz. The corresponding transmission coefficient $S_{21}$, extracted directly from the CST simulation, is illustr ated in Figure 12. Within this frequency range, $S_{21}$ remains near zero, spanning between −0.106 dB and −0.138 dB, indicative of minimal attenuation in the transmitted wave intensity. The parallel components of the relative permitti vity and permeability, namely $\varepsilon_r$ and $\mu_r$, within this frequency band reflect advantageous electromagnetic characteris tics. The absolute values of the complex relative permittivity and permeability, as calculated from the CST simulati on results, are graphed in Figure 14. For example, at 8.2 GHz, $\varepsilon_r = 3.698 - 0.081j$ and $\mu_r = 5.937 + 0.127j$, whereas at 9.5 GHz, $\varepsilon_r = 0.692 + 0.697j$ and $\mu_r = 1.400 - 0.987j$. The nearly comparable real and imaginary components of $\varepsilon_r$ at this frequency may be associated with enhanced dielectric loss mechanisms and interfacial polarization effects w ithin the heterogeneous nanocomposite structure. The observed decrease in the real parts alongside proportional inc reases in the imaginary parts signify beneficial electromagnetic response characteristics. In addition, the gradual var iation of $\varepsilon_r$ and $\mu_r$ across the investigated frequency range suggests a predominantly loss-governed electromagnetic r esponse, in which conductive dissipation through the MWCNT network and dielectric loss mechanisms are more in fluential than localized magnetic resonance effects. Consequently, the frequency response remains relatively smoot h with limited resonant features. Complementing these numerical results for $S_{11}$ and $S_{21}$, the parameters $S_{12}$ and $S_{22}$, which characterize coupling and port interaction, exhibit smooth yet nonlinear variations over the same frequency r ange without evidence of sharp resonant phenomena. The real and imaginary parts of all scattering parameters ($S_{11}$, $S_{21}$, $S_{12}$, and $S_{22}$) extracted from the CST simulations are collectively plotted in Figure 13. Notably, the real part of S $_{12}$ increases monotonically from approximately −0.75 at 8.2 GHz to zero near 10 GHz, eventually reaching about +0 .9 at 12.4 GHz. Conversely, the imaginary part of $S_{12}$ forms a broad convex curve, rising from roughly 0.70 at lower frequencies to approximately 0.95 between 9.5 and 10 GHz, before decreasing to about 0.40 at 12.4 GHz. In contras t, the real part of $S_{22}$ remains relatively stable throughout the band, slightly decreasing from 0.12 to 0.10, while the i maginary part of $S_{22}$ decreases approximately linearly in response to increasing impedance matching at the output p ort, from about +0.10 at 8.2 GHz to −0.25 at 12.4 GHz. Within the intermediate frequency band from 10 GHz to 11 GHz, the magnitude of $S_{11}$ increases gradually to −13.96 dB at 11 GHz, while $S_{21}$ exhibits only minor variation, ran ging from −0.151 dB to −0.117 dB. In parallel, $S_{12}$ and $S_{22}$ continue their nonlinear but smooth trends, further suppo rting the conclusion of stable impedance matching without abrupt discontinuities or resonance-induced fluctuations. At higher frequencies (11.5 GHz to 12.4 GHz), the magnitudes of $S_{11}$ and $S_{21}$ range from −13.65 to −13.14 dB and − 0.191 to −0.215 dB, respectively, confirming continued stable power transfer. Here, $S_{12}$ attains its maximum real va lues, and $S_{22}$ remains weakly dependent on frequency, collectively indicating effective signal isolation and port mat ching across the entire band. Simultaneously, $\varepsilon_r$ and $\mu_r$ demonstrate enhancements in their real parts along with incr eased variability in their imaginary parts; for instance, at 12.4 GHz, $\varepsilon_r = 3.777 + 0.820j$ and $\mu_r = 5.289 - j$. In summ ary, based on the values documented in Table 3 and the trends illustrated in Figures 11 to 14, which originate from t he CST simulation environment, the $S_{11}$ and $S_{21}$ parameters exhibit predominantly linear to quasi-linear behavior at t he macro scale. This behavior, together with the smooth evolution of $S_{12}$ and $S_{22}$ and the absence of abrupt oscillator y features, indicates a broadband and physically stable electromagnetic response throughout the entire frequency ra nge from 8.2 GHz to 12.4 GHz.

**Table. 3** Simulated electromagnetic Parameters of the Nanocomposite in the X-band Frequency Range

| Frequency (GHz) | $S_{11}$ (dB) | $S_{21}$ (dB) | $\varepsilon_r$ (Re ± j Im) | $\mu_r$ (Re ± j Im) |
|---|---|---|---|---|
| 8.2 | -16.17 | -0.106 | 3.698 – 0.081j | 5.937 + 0.127j |



[ DOI: 10.22068/ijmse.4568 ]

| | | | | |
|---|---|---|---|---|
| 8.5 | -15.92 | -0.113 | 2.908 + 0.187j | 4.832 – 0.231j |
| 9 | -15.45 | -0.125 | 1.681 + 0.513j | 3.127 – 0.685j |
| 9.5 | -15.04 | -0.138 | 0.692 + 0.697j | 1.400 – 0.987j |
| 10. | -14.66 | -0.151 | 0.137 – 0.734j | 0.291 + 1.067j |
| 10.5 | -14.30 | -0.164 | 0.870 – 0.627j | 1.850 + 0.903j |
| 11 | -13.96 | -0.117 | 1.565 – 0.386j | 3.180 + 0.533j |
| 11.5 | -13.65 | -0.191 | 2.274 – 0.031j | 4.208 + 0.040j |
| 12 | -13.36 | -0.205 | 3.058 + 0.420j | 4.924 – 0.462j |
| 12.4 | -13.14 | -0.215 | 3.777 + 0.820j | 5.289 – 0.803j |

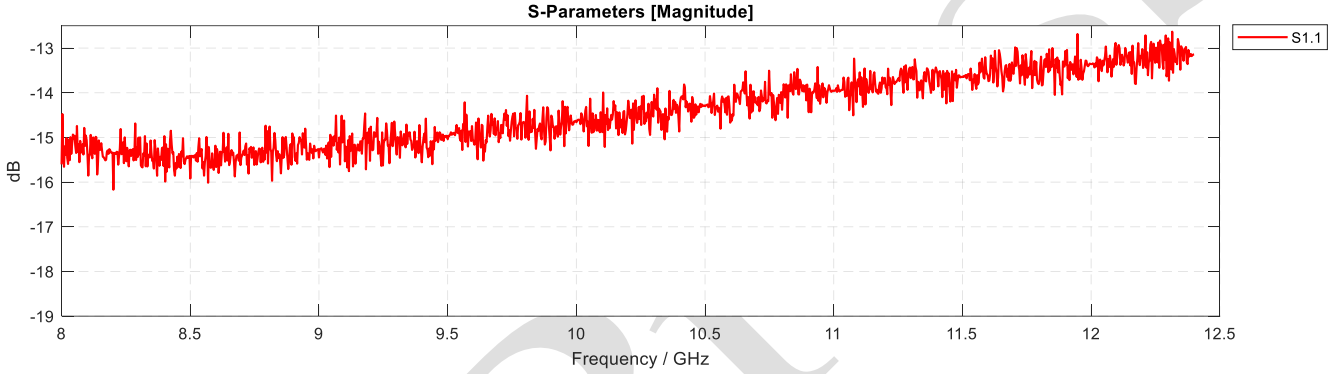


**Fig. 11.** Simulated reflection coefficient $S_{11}$ obtained from CST numerical analysis

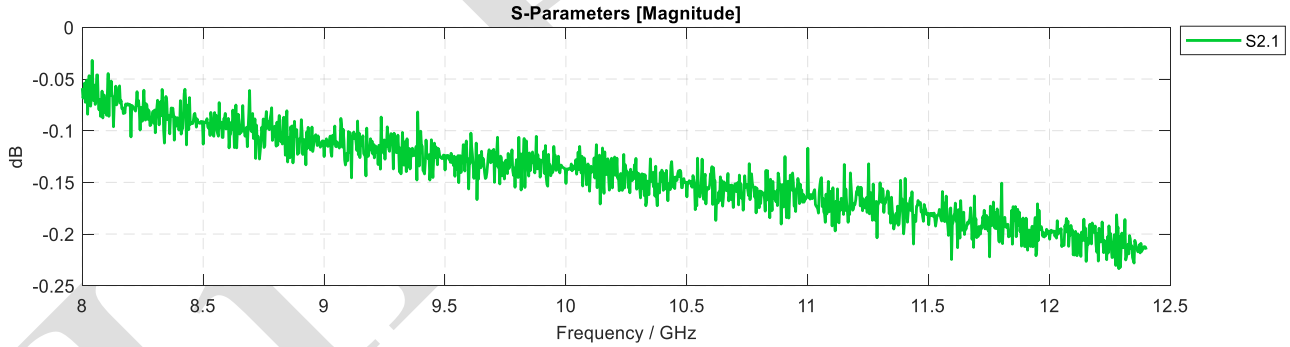


**Fig. 12.** Simulated transmission coefficient $S_{21}$ obtained from CST numerical analysis

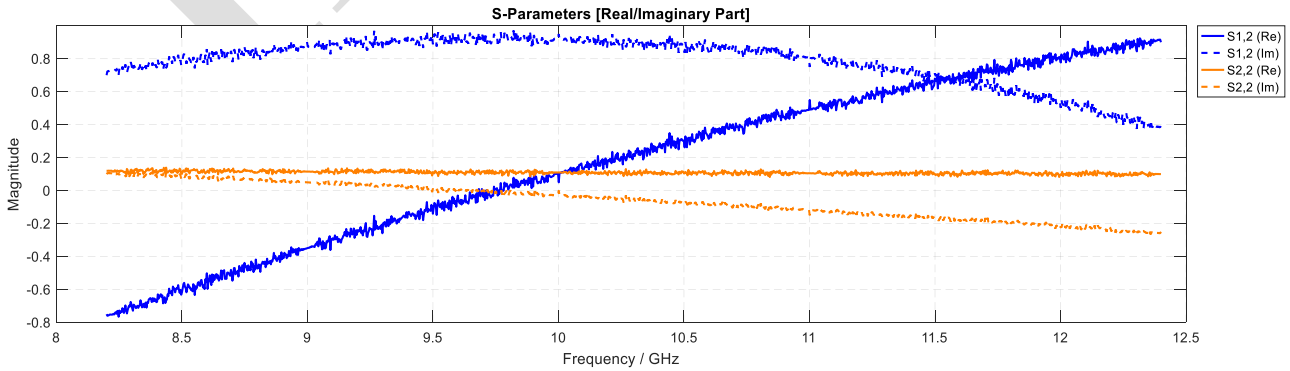


**Fig. 13.** Magnitude and phase (or real and imaginary components) of the S-parameters derived from CST simulation



[ DOI: 10.22068/ijmse.4568 ]

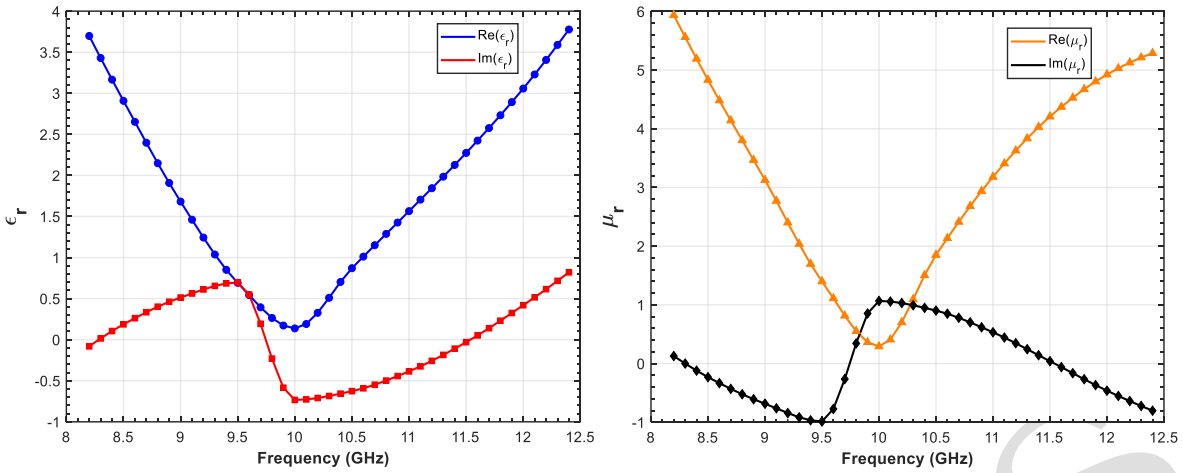


**Fig. 14.** Estimated magnetic permeability $\mu_r$ and electric permittivity $\varepsilon_r$ derived from CST numerical simulation results

## 7.2. RESULTS OF VNA SETUP

Analyzing the reflection loss (RL) and transmission parameters over the frequency range of 8.2–12.4 GHz, as summarized in Table 4, it is evident that increasing the $ZnTiO_3$ content in the samples leads to a gradual decrease in reflection loss accompanied by a concomitant suppression of transmission. This behavior indicates an improved impedance matching with the incident electromagnetic waves. The variation of reflection loss versus frequency is graphically depicted in Figs. 15 and 16 for the RL ($S_{11}$, dB) and Tr ($S_{21}$, dB) parameters, respectively.

At 8.2 GHz, sample C1 exhibits an RL of approximately −15.85 dB with transmission near −0.114 dB, while C2 shows an RL of about −16.80 dB with transmission around −0.092 dB. Sample C3 has an RL of approximately −17.10 dB with transmission close to −0.075 dB. Notably, sample C4 with the highest $ZnTiO_3$ concentration (19.67%) achieves an RL of about −17.85 dB with transmission near −0.072 dB, reflecting the best impedance matching performance within the set at this frequency. For intermediate frequencies such as 9.0 GHz, C1's RL is around −15.25 dB with transmission near −0.125 dB, whereas C4 records an RL near −17.25 dB with transmission approximately −0.078 dB. Similarly, at 9.5 GHz, C1 demonstrates an RL of about −14.95 dB with transmission around −0.138 dB, compared to The RL of Sample C4 of about −16.85 dB and transmission close to −0.080 dB. These data, as seen in Figs. 15 and 16, clearly demonstrate a progressive decline in reflection loss and transmission correlated with the increased $ZnTiO_3$ concentration. In the frequency band between 10 and 10.5 GHz, The RL of Sample C1 varies from −14.66 dB to −14.30 dB with transmission ranging from −0.151 dB to −0.164 dB. Conversely, C4 presents an RL from −16.50 dB to −16.10 dB accompanied by transmission between −0.082 dB and −0.090 dB. This trend reflects enhanced dielectric properties due to $ZnTiO_3$ incorporation, resulting in reduced surface reflection, while the decrease in transmission is attributed to scattering of local electromagnetic waves by MWCNT networks.

At higher frequencies (11–12.4 GHz), reflection loss becomes less negative across all samples but remains minimal for C4, which retains superior impedance matching. For instance, at 12 GHz, C1 has a reflection loss of approximately −13.36 dB and transmission of −0.205 dB, whereas C4 demonstrates values near −15.25 dB and −0.095 dB, respectively. These observations confirm, as illustrated in Figs. 15 and 16, the significant role of $ZnTiO_3$ in minimizing reflection loss and enhancing impedance matching, while $Fe_3O_4$ contributes primarily through magnetic loss mechanisms. A comprehensive review of RL and transmission values across the frequency spectrum indicates that C4 consistently exhibits the best performance by minimizing reflection and transmission, which corresponds to superior impedance matching close to unity. The MWCNTs act as effective scattering centers due to their partial electrical conductivity, particularly suppressing transmission in the mid-frequency band. $ZnTiO_3$ improves dielectric properties, and $Fe_3O_4$ introduces magnetic loss, jointly optimizing the electromagnetic response of the composite. In conclusion, sample C4 represents the most effective configuration in terms of electromagnetic wave suppression via impedance matching. The critical contribution of $ZnTiO_3$ in reducing reflection losses is complemented by enhancements in transmission suppression and bandwidth stability afforded by MWCNTs and $Fe_3O_4$. Conversely, samples with lower $ZnTiO_3$ content, such as C1, show higher transmission and less negative reflection losses, resulting in comparatively inferior overall performance.

**Table 4** Reflection loss (RL) and transmission of nanocomposite samples obtained from experimental VNA measurements



[ DOI: 10.22068/ijmse.4568 ]

| Freq (GHz) | RL C1 (dB) | Tr C1 (dB) | RL C2 (dB) | Tr C2 (dB) | RL C3 (dB) | Tr C3 (dB) | RL C4 (dB) | Tr C4 (dB) |
|---|---|---|---|---|---|---|---|---|
| 8.2 | -15.85 | -0.114 | -16.80 | -0.092 | -17.10 | -0.075 | -17.85 | -0.072 |
| 8.5 | -15.70 | -0.113 | -16.40 | -0.094 | -16.90 | -0.077 | -17.35 | -0.074 |
| 9.0 | -15.25 | -0.125 | -16.10 | -0.096 | -16.75 | -0.079 | -17.25 | -0.078 |
| 9.5 | -14.95 | -0.138 | -15.70 | -0.100 | -16.25 | -0.081 | -16.85 | -0.080 |
| 10.0 | -14.66 | -0.151 | -15.35 | -0.106 | -15.90 | -0.085 | -16.50 | -0.082 |
| 10.5 | -14.35 | -0.164 | -14.95 | -0.112 | -15.55 | -0.088 | -16.10 | -0.090 |
| 11.0 | -13.90 | -0.117 | -14.65 | -0.115 | -15.20 | -0.092 | -15.90 | -0.093 |
| 11.5 | -13.70 | -0.191 | -14.35 | -0.121 | -14.95 | -0.098 | -15.55 | -0.096 |
| 12.0 | -13.35 | -0.205 | -14.05 | -0.126 | -14.60 | -0.102 | -15.25 | -0.095 |
| 12.4 | -13.00 | -0.215 | -13.80 | -0.130 | -14.35 | -0.105 | -15.05 | -0.096 |

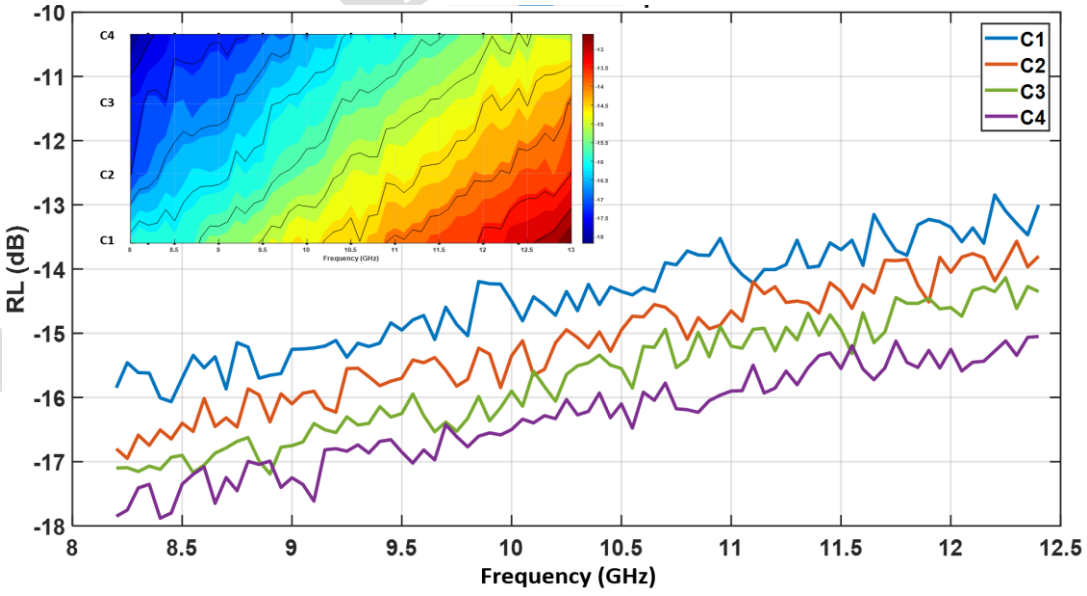


**Fig. 15.** Reflection Loss diagram in dB from experimental testing for nanocomposite samples



[ DOI: 10.22068/ijmse.4568 ]

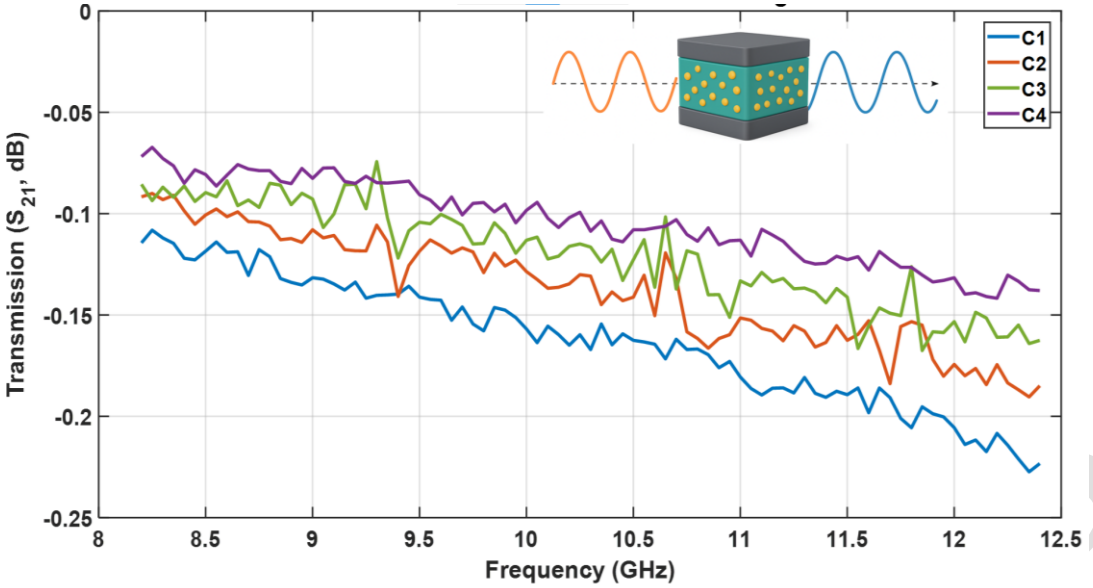


**Fig. 16.** Transmission diagram in dB from experimental testing for nanocomposite samples

### 7.3. VALIDATION

As presented in Table 5, the validation of the C4 nanocomposite absorber was performed by comparing the simulated $S_{11}$ reflection loss obtained from CST with the experimental values measured using a vector network analyzer (VNA). The CST results exhibit a nearly linear variation across the X-band frequency range (8.2–12.4 GHz), indicating the broadband absorption behavior of the designed nanocomposite. This smooth and quasi-linear response is mainly attributed to the combined dielectric and magnetic relaxation losses together with effective impedance matching, rather than sharp resonant attenuation mechanisms. The experimental VNA results show slight fluctuations throughout the frequency band, which are commonly observed in practical microwave measurements due to environmental noise, calibration limitations, connector losses, and sample inhomogeneity. Overall, the relative difference between CST and VNA results ranges from 8.24% to 12.69%. Although these percentage differences appear noticeable, the actual deviation in reflection loss remains relatively small, corresponding to approximately 1.5–2 dB over the investigated frequency range. To quantitatively evaluate the agreement between simulation and experiment, the statistical indices MAE and RMSE were calculated according to Eqs. (10-12), respectively.

$$MAE = \frac{1}{n}\sum_{i=1}^{n}|M_i - S_i| \tag{10}$$

$$RMSE = \sqrt{\frac{1}{n}\sum_{i=1}^{n}(M_i - S_i)^2} \tag{11}$$

$$MAPE = \frac{100}{n}\sum_{i=1}^{n}\left|\frac{M_i - S_i}{M_i}\right| \tag{12}$$

The obtained MAE and RMSE values are approximately 1.64 dB and 1.65 dB, while the mean absolute percentage error (MAPE) is about 11.06%. These results indicate a relatively consistent deviation between the simulated and measured responses. The simulation slightly overestimates the reflection loss across the entire frequency range, mainly because CST assumes an ideal homogeneous structure with perfectly dispersed fillers and uniform electromagnetic properties. In contrast, the fabricated samples may contain local agglomeration of $ZnTiO_3$, $Fe_3O_4$, and MWCNT nanoparticles, minor thickness variations, and non-uniform filler dispersion. Despite these differences, the numerical model successfully reproduces the overall broadband absorption trend and confirms that the dominant electromagnetic attenuation mechanisms are properly captured in the simulation.



[ DOI: 10.22068/ijmse.4568 ]

**Table. 5** Reflection values of sample C4 in experimental test and numerical simulation.

| Freq(GHz) | VNA Measurement | CST Simulation | Error (%) |
|---|---|---|---|
| 8.2 | -17.85 | -16.17 | 9.41 |
| 8.5 | -17.35 | -15.92 | 8.24 |
| 9.0 | -17.25 | -15.45 | 10.43 |
| 9.5 | -16.85 | -15.04 | 10.74 |
| 10.0 | -16.50 | -14.66 | 11.15 |
| 10.5 | -16.10 | -14.30 | 11.18 |
| 11.0 | -15.90 | -13.96 | 12.20 |
| 11.5 | -15.55 | -13.65 | 12.21 |
| 12.0 | -15.25 | -13.36 | 12.39 |
| 12.4 | -15.05 | -13.14 | 12.69 |

## 8. CONCLUSION

### 8.1. Design Strategy, Fabrication, and Performance Evaluation

The primary objective of this study was to systematically investigate impedance matching behavior and reflection reduction in $Fe_3O_4$/$ZnTiO_3$/MWCNT/epoxy microwave nanocomposites with varying $ZnTiO_3$ content, in order to clarify the specific role of $ZnTiO_3$ as a dielectric tuning phase. The experimental framework was designed using Response Surface Methodology (RSM), enabling controlled compositional variation, statistical evaluation of parameter sensitivity, and optimized selection of constituent ratios. $ZnTiO_3$ was considered the main variable, while MWCNT and $Fe_3O_4$ contents were maintained within relatively narrow ranges to preserve stable conductive and magnetic loss mechanisms and to avoid excessive percolation or dominant magnetic attenuation. This constrained design allowed the dielectric tuning effect of $ZnTiO_3$ on reflection characteristics to be clearly distinguished. The nanocomposites were fabricated under carefully controlled dispersion and curing conditions to achieve homogeneous filler distribution within the epoxy matrix. SEM analysis confirmed uniform nanoparticle dispersion, strong interfacial adhesion, and the formation of a hybrid conductive–magnetic network in which $Fe_3O_4$ and $ZnTiO_3$ nanoparticles were anchored onto the surfaces of MWCNTs. XRD results revealed reduced crystallinity and broadened diffraction peaks compared to individual phases, indicating nanoscale crystallite dimensions and interfacial strain within the composite structure. VSM measurements demonstrated a multiphase magnetic response predominantly governed by $Fe_3O_4$, while $ZnTiO_3$ and MWCNTs contributed to gradual magnetic variation and structural stabilization. Electromagnetic performance was evaluated in the X-band (8.2–12.4 GHz) experimentally using a calibrated waveguide–VNA setup and numerically using CST Microwave Studio. Effective electromagnetic parameters were modeled considering dielectric polarization, conductive percolation, and magnetic interactions. Both simulation and experimental results consistently showed broadband impedance matching and reflection reduction without sharp resonance peaks, leading to a smooth and quasi-linear frequency response dominated by distributed dielectric and conductive loss mechanisms. Among the investigated compositions (C1–C4), increasing the $ZnTiO_3$ content resulted in more effective impedance matching and more significant reflection reduction. The C4 sample, containing the highest $ZnTiO_3$ fraction, exhibited the best reflection performance and achieved a minimum reflection loss (RL) of −17.85 dB at 8.2 GHz, corresponding to a $ZnTiO_3$ content of 19.67 wt%. This result indicates a highly optimized impedance balance between the nanocomposite surface and free space. In contrast, samples with lower $ZnTiO_3$ content (C1–C3) demonstrated weaker impedance matching and less pronounced reflection reduction across the same frequency range. Although the presence of MWCNTs and $Fe_3O_4$ contributed to conductive and magnetic loss mechanisms, the insufficient dielectric contribution limited the overall impedance balance, preventing RL values comparable to those of C4. The progressive improvement from C1 to C4 confirms the critical role of $ZnTiO_3$ in dielectric tuning and impedance optimization within the composite system. Increasing its concentration enhances interfacial polarization and dielectric relaxation processes, facilitating better wave penetration into the structure and reduced surface reflection. Consequently, the synergistic interaction among the magnetic ($Fe_3O_4$), conductive (MWCNT), and dielectric ($ZnTiO_3$) phases leads to minimized reflection in the optimized composition. Validation analysis demonstrated good agreement between CST simulations and experimental VNA measurements, with MAE and RMSE values of approximately ~1.6 dB. Minor discrepancies are attributed to factors such as nanoparticle agglomeration, slight thickness variations, and calibration limitations. Nevertheless, the numerical model successfully reproduced the overall broadband reflection reduction trend, confirming that the electromagnetic behavior of the system is primarily governed by loss mechanisms and impedance matching rather than sharp resonance phenomena. The Flow chart diagram illustrated in Figure 7, shows a summary of the design process for this multiphase nanocomposite.



[ DOI: 10.22068/ijmse.4568 ]

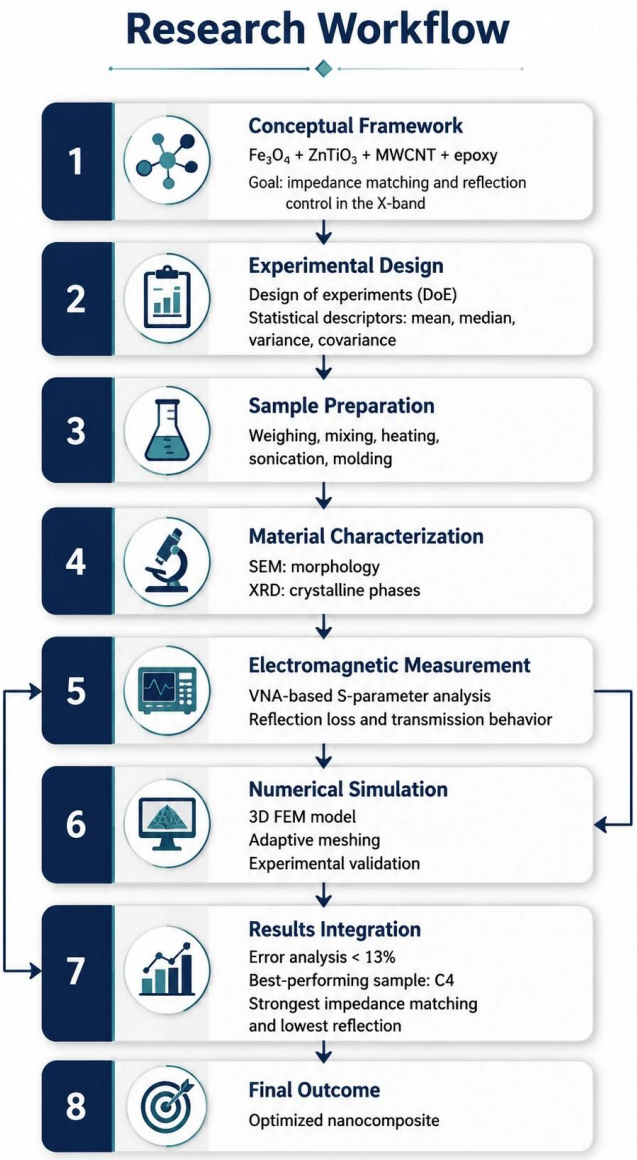


**Fig. 17.** Flow chart diagram of the design and optimization process of the nanocomposite

### 8.2. Limitations and Future works

Although the present study demonstrated noticeable reflection reduction and improved impedance matching behavior in the $Fe_3O_4$/$ZnTiO_3$/MWCNT/epoxy system, several inherent limitations warrant further consideration. The investigated compositions were restricted to relatively narrow filler concentrations to preserve homogeneous dispersion, structural integrity, and stable electromagnetic behavior. This deliberate constraint, while aiding in clarifying the role of $ZnTiO_3$, inherently limits the full exploration of the broader nonlinear interaction landscape between conductive, dielectric, and magnetic phases. Furthermore, all electromagnetic measurements were carried out using a single, fixed sample thickness, which critically restricts the accurate evaluation of thickness-dependent attenuation mechanisms such as quarter-wavelength cancellation, phase interference, and multiple internal reflections. Consequently, the current results primarily reflect the material's impedance matching and reflection suppression capability rather than its maximum achievable microwave absorption performance, making a precise quantification of energy dissipation challenging. Another significant limitation is that the electromagnetic characterization was performed using bulk waveguide-insert samples rather than real coating geometries deposited on metallic or dielectric substrates. In practical applications, substrate coupling effects, surface roughness, and coating uniformity can profoundly influence the overall electromagnetic attenuation behavior. Therefore, future investigations should prioritize comprehensive studies encompassing multiple sample thicknesses, broader



[ DOI: 10.22068/ijmse.4568 ]

compositional windows, and extended frequency bands beyond the X-band, notably into Ku-, K-, and Ka-band regions. Critically, evaluating these nanocomposites as applied coatings, possibly with multilayer or gradient-structured designs, under both waveguide and anechoic chamber conditions will provide a more realistic and technologically relevant performance assessment. Given the promising current results, this material system emerges as a strong candidate for X-band electromagnetic wave absorption, provided these more detailed explorations with variable parameters and a diversified range of material percentages are thoroughly conducted. Additionally, exploring hybridizations of $ZnTiO_3$ with other high-loss dielectric ceramics, advanced ferrites, MXenes, graphene-based materials, or conductive polymers could unlock superior synergistic loss mechanisms, paving the way for enhanced broadband absorption capabilities in advanced electromagnetic shielding and stealth applications.

## AWKNOWLEDGEMENT

This research was conducted using tools and equipment provided by the Faculty of Chemical, Electrical and Mechanical Engineering of Iran University of Science and Technology, as well as the Nanophysics Research Center of Shahid Sattari University of Aerospace Science and Technology.

## REFRENCES

[1] Khakbaz, M.; Javadi, M.; Sarkhosh, R. Investigation of Radar Reflectivity Reduction in Second-Degree Surfaces and Conic Sections Made of Aluminum in the X-Band Frequency Range: A Study Based on Electromagnetic Permittivity and Permeability. Mech. Struct. Fluids 2025, 15, 65–80. https://doi.org/10.22044/jsfm.2025.15682.3937 (In Persian).

[2] Yadav, R. S.; Kuřitka, I. Recent Advances in Outstanding Microwave Absorption and Electromagnetic Interference Shielding Nanocomposites of ZnO Semiconductor. Adv. Colloid Interface Sci. 2024, 326, 103137. https://doi.org/10.1016/j.cis.2024.103137.

[3] Chand, K.; Zhang, X.; Chen, Y. Recent Progress in MXene and Graphene-Based Nanocomposites for Microwave Absorption and Electromagnetic Interference Shielding. Arab. J. Chem. 2022, 15, 104143. https://doi.org/10.1016/j.arabjc.2022.104143.

[4] Qi, G.; Liu, Y.; Chen, L.; et al. Lightweight $Fe_3C$@Fe/C Nanocomposites Derived from Wasted Cornstalks with High-Efficiency Microwave Absorption and Ultrathin Thickness. Adv. Compos. Hybrid Mater. 2021, 4, 1226–1238. https://doi.org/10.1007/s42114-021-00368-0.

[5] Wang, J.; Sun, Q.; Li, J.; et al. Polymer-Based Nanocomposites: Role of Interface for Effective Microwave Absorption. Mater. Today Phys. 2023, 31, 100981. https://doi.org/10.1016/j.mtphys.2023.100981.

[6] Du, Y. Advances in Carbon-Based Microwave Absorbing Materials. Materials 2022, 15, 1359. https://doi.org/10.3390/ma15041359.

[7] Janem, N.; Azizi, Z. S.; Tehranchi, M. M. Microwave Absorption and Magnetic Properties of Thin-Film $Fe_3O_4$@Polypyrrole Nanocomposites: The Synthesis Method Effect. Synth. Met. 2021, 282, 116948. https://doi.org/10.1016/j.synthmet.2021.116948.

[8] Wang, H.; Hao, Y.; Xiang, L.; et al. Interface and Magnetic–Dielectric Synergy Strategy to Develop $Fe_3O_4$–$Fe_2CO_3$/MWCNT/rGO Mixed-Dimensional Multicomponent Nanocomposites for Microwave Absorption. Mater. Res. Bull. 2024, 171, 112631. https://doi.org/10.1016/j.materresbull.2023.112631.

[9] Bheema, R. K.; Etika, K. C. Large Microwave Absorption by $Fe_3O_4$@CuNW Hybrid Nanoparticles Filled Epoxy Nanocomposites in the X-Band. J. Alloys Compd. 2023, 938, 168405. https://doi.org/10.1016/j.jallcom.2022.168405.

[10] Govindasamy, T.; Mathew, N. K.; Asapu, V. K.; et al. Evaluating the Microwave Absorbing Performance of Polymer-Free Thin $Fe_3O_4$–MWCNT Nanocomposites in the X-Band Region. Surf. Interfaces 2023, 44, 103716. https://doi.org/10.1016/j.surfin.2023.103716.

[11] Du, B.; Zhang, G.; Huan, X.; et al. Electrostatically Self-Assembled $Fe_3O_4$@$SiO_2$/MXene 3D Interlayered Structure Improves Ku-Band Microwave Absorption Efficiency of Epoxy-Based Nanocomposites. Compos. Part A 2024, 177, 107956. https://doi.org/10.1016/j.compositesa.2023.107956.

[12] Huang, X.; Chen, Y.; Yu, J.; et al. Fabrication and Electromagnetic Loss Properties of $Fe_3O_4$ Nanofibers. J. Mater. Sci. Mater. Electron. 2015, 26, 3474–3478. https://doi.org/10.1007/s10854-015-2857-y.

[13] Koufakis, E.; Mathioudakis, G. N.; Patsidis, A. C.; Psarras, G. C. $ZnTiO_3$/Epoxy Resin Nanocomposites: Development, Dielectric Behaviour and Functionality. Polym. Test. 2019, 77, 105870. https://doi.org/10.1016/j.polymertesting.2019.04.017.



[ DOI: 10.22068/ijmse.4568 ]

[14] Wattanawikkam, C.; Pecharapa, W. Optical, Dielectric and Photocatalytic Properties of Perovskite $ZnTiO_3$ Nanoparticles Synthesized by Sonochemical Process. IEEE Int. Symp. Appl. Ferroelectr. 2015, 280–283. https://doi.org/10.1109/ISAF.2015.7172726.
[15] Nahrawy, A. M. E.; Hammad, A. B. A.; Bakr, A. M.; et al. Adjustment of Morphological and Dielectric Properties of $ZnTiO_3$ Nanocrystalline Using $Al_2O_3$ Nanoparticles. Appl. Phys. A 2019, 125, 54. https://doi.org/10.1007/s00339-018-2350-6.
[16] Kim, H.; Byun, J.; Kim, Y. Microstructure and Microwave Dielectric Properties of Modified Zinc Titanates (I). Mater. Res. Bull. 1998, 33, 963–973. https://doi.org/10.1016/S0025-5408(98)00056-7.
[17] Gonzales, L. L.; Hartwig, M. S.; Fassbender, R. U.; et al. Properties of Zinc Titanates Synthesized by Microwave-Assisted Hydrothermal Method. Heliyon 2021, 7, e06521. https://doi.org/10.1016/j.heliyon.2021.e06521.
[18] Salavati-Niasari, M.; Soofivand, F.; Sobhani-Nasab, A.; et al. Synthesis, Characterization, and Morphological Control of $ZnTiO_3$ Nanoparticles through Sol–Gel Processes and Their Photocatalyst Application. Adv. Powder Technol. 2016, 27, 2066–2075. https://doi.org/10.1016/j.apt.2016.07.018.
[19] Chang, Y.; Chang, Y.; Chen, I.; Chen, G.; Chai, Y. Synthesis and Characterization of Zinc Titanate Nanocrystal Powders by Sol–Gel Technique. J. Cryst. Growth 2002, 243, 319–326. https://doi.org/10.1016/S0022-0248(02)01490-2.
[20] Shahriyari, S.; Omidi, M.; Hassanzadeh-Tabrizi, S. A.; et al. Electromagnetic Wave Absorption of Epoxy Resin–MWCNT Composites Synthesized via Ultrasonic Bath and Milling Process. J. Adv. Mater. Process. 2022, 10, 3–12.
[21] Wang, L.; Qiu, H.; Liang, C.; Song, P. Electromagnetic Interference Shielding MWCNT–$Fe_3O_4$@Ag/Epoxy Nanocomposites with Satisfactory Thermal Conductivity and High Thermal Stability. Carbon 2018, 141, 506–514. https://doi.org/10.1016/j.carbon.2018.10.003.
[22] Zhang, L.; Feng, H.; Lv, J.; et al. Facile Fabrication of PPy/MWCNTs Composites with Tunable Dielectric Properties and Their Superior Electromagnetic Wave Absorbing Performance. J. Polym. Res. 2024, 31, 354. https://doi.org/10.1007/s10965-024-04189-9.
[23] Zhang, A.; Wang, D.; Li, Y.; et al. The Effect of Microspheres Surface Morphology on the Enhanced Microwave Absorbing Properties of MWCNTs. J. Polym. Res. 2021, 28, 91. https://doi.org/10.1007/s10965-020-02303-1.
[24] Angiulli, G.; Versaci, M. Retrieving the Effective Parameters of an Electromagnetic Metamaterial Using the Nicolson–Ross–Weir Method: An Analytic Continuation Problem along the Path Determined by Scattering Parameters. IEEE Access 2021, 9, 77511–77525. https://doi.org/10.1109/ACCESS.2021.3082261.
[25] Angiulli, G.; Versaci, M. Extraction of the Electromagnetic Parameters of a Metamaterial Using the Nicolson–Ross–Weir Method: An Analysis Based on Global Analytic Functions and Riemann Surfaces. Appl. Sci. 2022, 12, 11121. https://doi.org/10.3390/app122111121.
[26] Peña-Rodríguez, G.; Duan, G.; Vera-Barrera, R.; et al. Electromagnetic Properties of a Magneto-Dielectric Composed through an Algorithm Based on the Nicolson–Ross–Weir Method. Rev. Ing. Investig. Desarro. 2021, 21, 59–69. https://doi.org/10.19053/1900771X.v21.n1.2021.13515.
[27] Sarkhosh, R.; Kazemi Nasrabadi, M.; Parsafar, R. Investigation of the Effect of Silica Foam Nanoparticles on the Mechanical, Electrical, and Magnetic Properties of Epoxy/Silica Foam Polymer Composites. Iran. J. Manuf. Eng. 2024, 11, 37–57. https://doi.org/10.22034/ijme.2024.426954.1879 (In Persian).
[28] Manesh, H.; Genoulaz, J.; Kameni, A.; et al. Experimental Analysis and Modelling of Coaxial Transmission Lines with Soft Shield Defects. IEEE Int. Symp. Electromagn. Compat. 2015, 1553–1558. https://doi.org/10.1109/ISEMC.2015.7256406.
[29] Li, Y.; Duan, Y.; Wang, C. Enhanced Microwave Absorption and Electromagnetic Properties of Si-Modified rGO@$Fe_3O_4$/PVDF-co-HFP Composites. Materials 2020, 13, 933. https://doi.org/10.3390/ma13040933.
[30] Zamani, K.; Tavoosi, M.; Ghasemi, A. Electromagnetic Behavior of in Situ Synthesized MXene-Based $Ti_3C_2/TiO_2$ Composites. Iran. J. Mater. Sci. Eng. 2025, 22, 14–23. https://doi.org/10.22068/ijmse.4035.
[31] Beddiaf, A.; Medjaldi, M.; Lanani, A.; et al. Investigation of Deposition Rates in Bilayer Silicon Nitride Structures Using Ellipsometry and the Maxwell Garnett Model. Russ. Microelectron. 2025, 54, 208–215. https://doi.org/10.1134/S1063739724600973.
[32] Zhu, S.; Wu, S.; Fu, Y.; Guo, S. Prediction of Particle-Reinforced Composite Material Properties Based on an Improved Halpin–Tsai Model. AIP Adv. 2024, 14, 045339. https://doi.org/10.1063/5.0206774.



[ DOI: 10.22068/ijmse.4568 ]